Evolutionary Game Theory: non-equilibrium and non-linear dynamics of interacting particle systems

Erwin Frey

Arnold Sommerfeld Center for Theoretical Physics
Ludwig-Maximilians-Universität München

Contents

1 Introduction **1**
- 1.1 Strategic games . . . 1
- 1.2 Evolutionary game theory . . . 3
- 1.3 Bacterial games . . . 6
- 1.4 Nonlinear dynamics of two-player games . . . 7
- 1.5 Some elementary notes on extinction times . . . 9

2 The May-Leonard model **13**
- 2.1 Linear stability analysis: Jordan normal form . . . 14
- 2.2 Invariant manifold . . . 16
- 2.3 Normal form . . . 17

3 Spatial Games with Cyclic Dominance **21**
- 3.1 Simulation results for the lattice gas model . . . 22
- 3.2 Reaction-diffusion equations . . . 24
  - 3.2.1 The linear spreading velocity . . . 24
  - 3.2.2 Wavelength and frequency . . . 26
- 3.3 The role of noise . . . 27
  - 3.3.1 Kramers-Moyal expansion of the reaction terms . . . 28
  - 3.3.2 Kramers-Moyal expansion of the diffusion term . . . 30
  - 3.3.3 Stochastic partial differential equations . . . 30
  - 3.3.4 The spirals' velocities, wavelengths, and frequencies . . . 33
  - 3.3.5 Scaling relation and critical mobility . . . 35
- 3.4 Discussion . . . 36

Chapter 1

Introduction

1.1 Strategic games

Classical Game Theory describes the behavior of rational players. It attempts to mathematically capture behavior in strategic situations, in which an individual's success in making choices depends on the choices of others. A classical example of a strategic game is the *prisoner's dilemma*. In its classical form, it is presented as follows:

"Two suspects of a crime are arrested by the police. The police have insufficient evidence for a conviction, and, having separated both prisoners, visit each of them to offer the same deal. If one testifies (defects from the other) for the prosecution against the other and the other remains silent (cooperates with the other), the betrayer goes free and the silent accomplice receives the full 10-year sentence. If both remain silent, both prisoners are sentenced to only 1 year in jail for a minor charge. If each betrays the other, each receives a five-year sentence. Each prisoner must choose to betray the other or to remain silent. Each one is assured that the other would not know about the betrayal before the end of the investigation. How should the prisoners act?"

The situation is best illustrated in what is called a "payoff matrix" which in the classical formulation is rather a "cost matrix":

P	Cooperator (C)	Defector (D)
C	1 year	10 years
D	0 years	5 years

Here rows and columns correspond to player (suspect) 1 and 2, respectively. The entries give the prison sentence for player 1; this is sufficient information since the game is symmetric. Imagine you are player 1, and that player 2 is playing strategy "cooperate". Then you are obviously better off to play "defect" since you can get free. Now imagine player 2 is playing "defect". Then you are still better off to defect since 5 years in prison is better than 10 years in prison. If both players are rational players a dilemma arises since both will analyze the situation in the same way and come to the conclusion that it is always better to play "defect" irrespective of what the other suspect is playing. This outcome of

the game, both playing "defect", is called a Nash equilibrium. The hallmark of a Nash equilibrium is that none of the players has an advantage of deviating from his strategy unilaterally. This rational choice, where each player maximizes his own payoff, is not the best outcome! If both defect, they will both be sentenced to prison for 5 years. Each player's individual reward would be greater if they both played cooperatively; they would both only be sentenced to prison for 1 year.

We can also reformulate the prisoner's dilemma game as follows. A cooperator provides a benefit b to another individual, at a cost c to itself (with $b-c>0$). In contrast, a defector refuses to provide any benefit and hence does not pay any costs. For the selfish individual, irrespective of whether the partner cooperates or defects, defection is favorable, as it avoids the cost of cooperation, exploits cooperators, and ensures not to become exploited. However, if all individuals act rationally and defect, everybody is, with a gain of 0, worse off compared to universal cooperation, where a net gain of $b-c$ would be achieved. The prisoner's dilemma therefore describes, in its most basic form, the fundamental problem of establishing cooperation.

P	Cooperator (C)	Defector (D)
C	$b-c$	$-c$
D	b	0

This scheme can be generalized to include other basic types of social dilemmas. Namely, two cooperators that meet are both *rewarded* a payoff $\mathcal{R}$, while two defectors obtain a *punishment* $\mathcal{P}$. When a defector encounters a cooperator, the first exploits the second, gaining the *temptation* $\mathcal{T}$, while the cooperator only gets the *suckers payoff* $\mathcal{S}$. Social dilemmas occur when $\mathcal{R}>\mathcal{P}$, such that cooperation is favorable in principle, while temptation to defect is large: $\mathcal{T}>\mathcal{S}$, $\mathcal{T}>\mathcal{P}$. These interactions may be

P	Cooperator (C)	Defector (D)
C	$\mathcal{R}$	$\mathcal{S}$
D	$\mathcal{T}$	$\mathcal{P}$

Variation of the parameters $\mathcal{T}$, $\mathcal{P}$, $\mathcal{R}$ and $\mathcal{S}$ yields four principally different types of games. The *prisoner's dilemma* arises if the temptation $\mathcal{T}$ to defect is larger than the reward $\mathcal{R}$, and if the punishment $\mathcal{P}$ is larger than the suckers payoff $\mathcal{S}$. As we have already seen above, in this case, defection is the best strategy for the selfish player. Within the three other types of games, defectors are not always better off. For the *snowdrift game* the temptation $\mathcal{T}$ is still higher than the reward $\mathcal{R}$ but the sucker's payoff $\mathcal{S}$ is larger than the punishment $\mathcal{P}$. Therefore, now actually cooperation is favorable when meeting a defector, but defection still pays off when encountering a cooperator, and a rational strategy consists of a mixture of cooperation and defection. The snowdrift game derives its name from the potentially cooperative interaction present when two drivers are trapped behind a large pile of snow, and each driver must decide whether to clear a path. Obviously, then the optimal strategy is the opposite of the opponent's (cooperate when your opponent defects and defect when your opponent cooperates). Another scenario is the *coordination game*, where mutual agreement is preferred: either all individuals cooperate or defect as the reward $\mathcal{R}$ is higher than the temptation $\mathcal{T}$ and the punishment $\mathcal{P}$ is higher than sucker's

payoff $\mathcal{S}$. Last, the scenario of *by-product mutualism* yields cooperators fully dominating cooperators since the reward $\mathcal{R}$ is higher than the temptation $\mathcal{T}$ and the sucker's payoff $\mathcal{S}$ is higher than the punishment $\mathcal{P}$.

1.2 Evolutionary game theory

Strategic games, as discussed in the previous section, are a useful concept in economic and social settings. In order to analyze the behavior of biological systems, the concept of rationality is not meaningful. Evolutionary game theory (EGT) as developed mainly by Maynard Smith and Price does not rely on rationality assumptions but on the idea that evolutionary forces like natural selection and mutation are the driving forces of change. The interpretation of game models in biology is fundamentally different from strategic games in economics or social sciences. In biology strategies are considered to be inherited programs which control the individual's behavior. Typically one looks at a population composed of individuals with different strategies who interact generation after generation in game situations of the same type. The interactions may be described by deterministic rules or stochastic processes, depending on the particular system under study. The ensuing dynamic process can then be viewed as an iterative (nonlinear) map or a stochastic process (either with discrete or continuous time). This naturally puts evolutionary game theory in the context of nonlinear dynamics and the theory of stochastic processes. We will see how a combination of both approaches helps to understand the emergence of complex spatio-temporal dynamics.

In this section, we focus on a *deterministic description of well-mixed populations*. The term "well-mixed" signifies systems where the individual's mobility (or diffusion) is so large that one may neglect any spatial degrees of freedom and assume that every individual is interacting with everyone at the same time. This is a mean-field picture where the interactions are given in terms of the average number of individuals playing a particular strategy. Frequently, this situation is visualized as an "urn model", where two (or more) individuals from a population are randomly selected to play with each other according to the specified game theoretical scheme. The term "deterministic" means that we are seeking a description of populations where the number of individuals $N_i(t)$ playing a particular strategy A_i are macroscopically large.

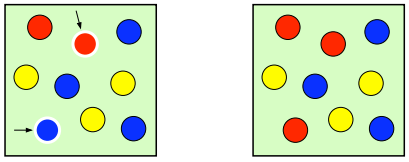

Figure 1.1: The urn model describes the evolution of well-mixed finite populations. We show three species as yellow (A), red (B), and blue (C) spheres. At each time step, two randomly selected individuals are chosen (indicated by arrows in the left picture) and interact with each other according to the rules of the game (right picture).

Let the state of the system at time t be given by the fractions (frequencies) $a_i(t) = N_i(t)/N(t)$ of different strategies A_i, summarized as a state vector $\vec{a} = (a_1, a_2, ..., a_d)$ with $\sum_{i=1}^{d} a_i = 1$; the ensuing $d-1$ dimensional phase space is called a simplex S_d (see Fig.**??** showing a S_3 simplex). The total population size $N(t) = \sum_{i=1}^{d} N_i(t)$ is frequently assumed to remain constant in time.

Pairwise reactions and rate equations

In the simplest setup the interaction between individuals playing different strategies can be represented as a reaction process characterized by some set of rate constants. For example, consider a game where three strategies $\{A, B, C\}$ cyclically dominate each other, as in the famous rock-paper-scissors game. In an evolutionary setting, the game is played according to an urn model as illustrated in Fig.1.1: at a given time t two individuals from a population with constant size N are randomly selected to play with each other (react) according to the scheme

$$\begin{aligned} A + B &\xrightarrow{k_A} A + A\,, \\ B + C &\xrightarrow{k_B} B + B\,, \\ C + A &\xrightarrow{k_C} C + C\,, \end{aligned} \tag{1.1}$$

where k_i are rate constants, i.e. probabilities per unit time. The ensuing rate equations read

$$\begin{aligned} \partial_t a &= a(k_A b - k_C c)\,, \\ \partial_t b &= b(k_B c - k_A a)\,, \\ \partial_t c &= c(k_C a - k_B b)\,, \end{aligned} \tag{1.2}$$

where the right hand side gives the balance of "gain" and "loss" processes. In writing these equations we have assumed that the number of individuals playing a particular strategy is macroscopic, $N_i \gg 1$.

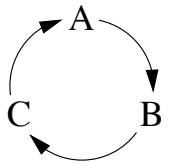

Figure 1.2: Illustration of cyclic dominance of three states A, B, and C.

The concept of fitness and replicator equations

In general, the situation in game theory is more complex such that a description by chemical reactions is not sufficient and it is less obvious how to set up a deterministic description. For illustration, consider a two-player game characterized by a payoff matrix $\mathbf{P}$:

$\mathbf{P}$	A	B
A	$p_{11} := \mathcal{R}$	$p_{12} := \mathcal{S}$
B	$p_{21} := \mathcal{T}$	$p_{22} := \mathcal{P}$

We define the frequencies

$$a = \frac{N_A}{N}\,, \tag{1.3}$$

$$b = \frac{N_B}{N} = (1-a)\,, \tag{1.4}$$

where N_A and N_B are the number of individuals playing strategy A and B, respectively, and $N = N_A + N_B$. In order to set up an equation of motion we now need a measure for the "fitness" of individuals playing a particular strategy, where the term "fitness" is - as usual - used synonymously for reproductive success. We define the fitness f_i of an individual playing strategy A_i as the expected payoff for that strategy

$$f_A(a) := \mathcal{R}a + \mathcal{S}(1-a)\,, \tag{1.5}$$

$$f_B(a) := \mathcal{T}a + \mathcal{P}(1-a)\,. \tag{1.6}$$

One now argues that rate of growth $(\dot{a}/a)$ of strategy A in the population is proportional to the surplus of its fitness with respect to the average fitness $\bar{f}(a) = af_A(a) + (1-a)f_B(a)$. The ensuing differential equation is known as the *standard replicator equation*

$$\partial_t a = \left[f_A(a) - \bar{f}(a)\right] a\,. \tag{1.7}$$

This equation guarantees that individuals using strategies with a fitness larger than the average fitness increase while those using strategies with a fitness below average decline in number. Without a more precise description of the type of "interactions" responsible for the time evolution of the population there is, of course, plenty of freedom in how to write down a differential equation describing the deterministic time evolution of the population. Indeed, there is another set of equations frequently used in EGT, called *adjusted replicator equations*, which reads

$$\partial_t a = \frac{f_A(a) - \bar{f}(a)}{\bar{f}(a)}\, a\,. \tag{1.8}$$

Here we will not bother to argue why one or the other is a better description. As we will see later, these equations emerge quite naturally from a full stochastic description in the limit of large populations.

It is obvious how to generalize these ideas to d strategies, defined in terms of a payoff matrix $\mathbf{P}$. Then the replicator equations read

$$\partial_t a_i = \left[f_i(\vec{a}) - \bar{f}(\vec{a})\right] a_i\,, \tag{1.9}$$

where we have defined

$$\vec{f} = \mathbf{P}\vec{a}\,, \tag{1.10}$$

$$\bar{f}(\vec{a}) = \sum_i f_i a_i\,. \tag{1.11}$$

1.3 Bacterial games

Recommended reading:

- Gore, J., H. Youk, and A. van Oudenaarden. *Snowdrift game dynamics and facultative cheating in yeast.* Nature 459, 253-256 (2009).
- Sinervo, B., and C.M. Lively. *The rock-paper-scissors game and the evolution of alternative male strategies.* Nature 380, 240-243 (1996).
- Kerr, B. et al. *Local dispersal promotes biodiversity in a real-life game of rock-paper-scissors.* Nature 418,171-174 (2002).

It is quite likely that microbal model systems will play a major role in our understanding of mechanisms driving evolutionary dynamics.

1.4 Nonlinear dynamics of two-player games

This section is intended to give a concise introduction into elementary concepts of nonlinear dynamics. We illustrate those for the replicator dynamics of two-player games characterized in terms of the payoff matrix

P	A	B
A	$\mathcal{R}$	$\mathcal{S}$
B	$\mathcal{T}$	$\mathcal{P}$

and the replicator dynamics

$$\begin{aligned} \partial_t a &= a(f_A - \bar{f}) = a\big(bf_A - [af_A + (1-a)f_B]\big) \\ &= a(1-a)(f_A - f_B)\,. \end{aligned} \tag{1.12}$$

This equation has a simple interpretation: the first factor, $a(1-a)$, is the probability for A and B to meet and the second factor, $f_A - f_B$, is the fitness advantage of A over B. Inserting the explicit expressions for the fitness values one finds

$$\partial_t a = a(1-a)\big[\mu_A(1-a) - \mu_B a\big] =: F(a)\,, \tag{1.13}$$

where μ_A is the relative benefit of A playing against B and μ_B is the relative benefit of B playing against A:

$$\mu_A := \mathcal{S} - \mathcal{P}\,, \qquad \mu_B := \mathcal{T} - \mathcal{R}\,. \tag{1.14}$$

Hence, as far as the replicator dynamics is concerned, we may replace the payoff matrix by

P	A	B
A	1	$1+\mu_A$
B	$1+\mu_B$	1

Eq.1.13 is a one-dimensional nonlinear first-oder differential equation for the fraction a of players A in the population. Graphically it is now trivial to characterizes its dynamics. The sign of $F(a)$ determines the increase or decrease of the dynamic variable a. compare the right half of Fig.1.3. The intersections of $F(a)$ with the a-axis (zeros) are *fixed points*, a^*. Generically, these intersections are with a finite slope $F'(a^*) \neq 0$; a negative slope indicates a stable fixed point while a positive slope an unstable fixed point. Depending on some *control parameters*, here μ_A and μ_B, the first or higher order derivatives of F at the fixed points may vanish. These special parameter values mark "threshold values" for changes in the flow behaviour ($\rightarrow$ *bifurcations*) of the nonlinear dynamics.

For the prisoner's dilemma $\mu_A < 0$ and $\mu_B > 0$ (see table 1.1) and hence player B is always better off (compare the payoff matrix). Both players playing strategy B is a Nash equilibrium. In terms of the replicator equations this situation corresponds to $F(a) < 0$ for $a \neq 0$ and $F(a) = 0$ at $a = 0, 1$ such that $a^* = 0$ is the only stable fixed point. Hence the term "Nash equilibrium" translates into the "stable fixed point" of the replicator dynamics (nonlinear dynamics).

For the snowdrift game both $\mu_A > 0$ and $\mu_B > 0$ such that $F(a)$ can change sign for $a \in [0,1]$. In fact, $a^*_{\rm int} = \mu_A/(\mu_A + \mu_B)$ is a stable fixed point while

Game	Control Parameters	Fixed Points a^*
prisoner's dilemma	$\mu_A < 0$; $\mu_B > 0$	0
snowdrift	$\mu_A > 0$; $\mu_B > 0$	$\mu_A/(\mu_A + \mu_B)$ stable
coordination	$\mu_A < 0$; $\mu_B < 0$	0, 1
harmony	$\mu_A > 0$; $\mu_B < 0$	1

Table 1.1: Classification of two player games according to their payoff matrices and fixed point values.

$a^* = 0, 1$ are unstable fixed points; see the right panel of Fig.1.3. Inspection of the payoff matrix tells us that it is always better to play the opposite strategy of your opponent. Hence there is no Nash equilibrium in terms of pure strategies A or B. This corresponds to the fact that the boundary fixed points $a^* = 0, 1$ are unstable. There is, however, a Nash equilibrium with a *mixed strategy* where a rational player would play strategy A with probability $p_A = \mu_A/(\mu_A + \mu_B)$ and strategy B with probability $p_B = 1 - p_A$. Hence, again, the term "Nash equilibrium" translates into the "stable fixed point" of the replicator dynamics (nonlinear dynamics).

For the coordination game, there is also an interior fixed point at $a^*_{\rm int} = \mu_A/(\mu_A + \mu_B)$, but now it is unstable, while the fixed points at the boundaries $a^* = 0, 1$ are stable. Hence we have *bistability*: for initial values $a < a^*_{\rm int}$ the flow is towards $a = 0$ while it is towards $a = 1$ otherwise. In the terminology of strategic games there are two Nash equilibria. The game harmony corresponds to the prisoner's dilemma with the roles of A and B interchanged.

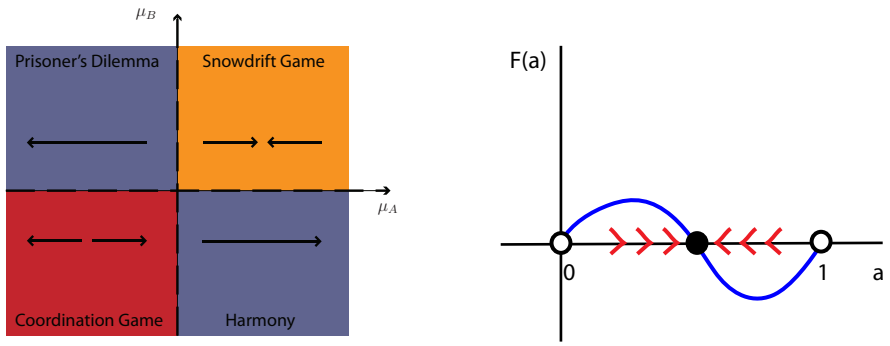

Figure 1.3: Classification of two-player games. *Left:* The black arrows in the control parameter plane (μ_A, μ_B) indicate the flow behavior of the four different types of two-player games. *Right:* Graphically the solution of a one-dimensional nonlinear dynamics equation, $\partial_t a = F(a)$, is simply read off from the signs of the function $F(a)$; illustration for the snowdrift game.

1.5 Some elementary notes on extinction times

Processes encountered in biological systems are often stochastic. For example, consider the degradation of a protein or the death of an individual bacterium in a population, and describe it as a stochastic event happening at a probability per unit time (rate) λ. Then the population size $N(t)$ at time t becomes a random variable, and its time evolution becomes a set of integers $\{N_\alpha\}$ changing from N_α to $N_\alpha - 1$ at particular times t_α; this is also called a realization of the stochastic process. Now it is no longer meaningful to ask for *the* time evolution of a particular population, as one would do in a deterministic description in terms of a rate equation, $\dot{N} = -\lambda N$. Instead one studies the time evolution of an ensemble of systems or tries to understand the distribution of times $\{t_\alpha\}$. A central quantity in this endeavor is the probability $P(N,t)$ to find a population of size N given that at some time $t = 0$ there was an initial ensemble of populations. Assuming that the stochastic process is Markovian, its dynamics is given by the following master equation:

$$\partial_t P(N,t) = \lambda(N+1)P(N+1,t) - \lambda N P(N,t)\,. \tag{1.15}$$

Such an equation can be analyzed by standard tools from the theory of stochastic processes. In particular, it can be solved exactly using generating functions. In this section we are only interested in the average extinction time T, i.e. the expected time for the population to reach the state $N = 0$, also called an *absorbing state*. This can be obtained rather easily by considering the probability $Q(t)$ that a given individual is still alive at time t given that it was alive at time $t = 0$. We immediately obtain

$$Q(t+dt) = Q(t)(1-\lambda t) \quad \text{with} \quad Q(0) = 1 \tag{1.16}$$

since an individual will be alive at time $t + dt$ if it was alive at time t and did not die within the time interval $[t, t + dt]$. The ensuing differential equation, $\dot{Q} = -\lambda Q$ is solved by $Q(t) = e^{-\lambda t}$. This identifies $\tau = 1/\lambda$ as the expected waiting time for a particular individual to die. We conclude that the waiting times for the population to change by one individual is distributed exponentially and its expected value is $\tau_N = \tau/N$ for a population of size N; note that each individual in a population has the same chance to die. Hence we can write for the expected extinction time for a population with initial size N_0

$$T = \tau_{N_0} + \tau_{N_0-1} + \cdots + \tau_1 = \sum_{N=1}^{N_0} \frac{\tau}{N} \approx \tau \int_1^{N_0} \frac{1}{N}\, dN = \tau \ln N_0\,. \tag{1.17}$$

We have learned that for a system with a "drift" towards the absorbing boundary of the state space the expected time to reach this boundary scales only logarithmically in the initial population size, $T \sim \ln N_0$. Note that within a deterministic description, $\dot{N} = -\lambda N$, the population size would exponentially decay to zero but never reach it, $N(t) = N_0 e^{-t/\tau}$. This is, of course, flawed in two ways. First, the process is not deterministic and, second, the population size is not a real number. Naively, one may estimate the extinction time by $N(T) = 1$, and indeed this gives $T = \tau \ln N_0$.

Now we would like to contrast the linear death process with a "neutral process" where death and birth events balance each other, i.e. the birth rate μ

equals the death rate λ. In a deterministic description one would write

$$\partial_t N(t) = -(\lambda - \mu)N(t) = 0 \tag{1.18}$$

and conclude that the population size remains constant at its initial value. In a stochastic description, one starts from the master equation

$$\partial_t P(N,t) = \lambda(N+1)P(N+1,t) + \lambda(N-1)P(N-1,t) - 2\lambda N P(N,t)\,. \tag{1.19}$$

Though this could again be solved exactly using generating functions it is instructive to derive an approximation valid in the limit of a large population size, i.e. $N \gg 1$. This is most easily done by simply performing a second order Taylor expansion without worrying to much about the mathematical validity of such an expansion. With

$$\big[(N \pm 1)P(N \pm 1,t)\big] \approx NP(N,t) \pm \partial_N\big[NP(N,t)\big] + \frac{1}{2}\partial_N^2\big[NP(N,t)\big] \tag{1.20}$$

we obtain

$$\partial_t P(N,t) = \lambda \partial_N^2\big[NP(N,t)\big]\,. \tag{1.21}$$

Measuring the population size in units of the initial population size at time $t = 0$ and defining $x = N/N_0$, this becomes

$$\partial_t P(x,t) = D\partial_x^2\big[xP(x,t)\big]\,. \tag{1.22}$$

where the "diffusion constant" $D = \lambda/N_0$[1]. This implies that all time scales in the problem scale as $t \sim D^{-1} \sim N_0$; this is easily seen by introducing a dimensionless time $\tau = Dt$ resulting in a rescaled equation

$$\partial_\tau P(x,\tau) = \partial_x^2\big[xP(x,\tau)\big]\,. \tag{1.23}$$

Hence for a (deterministically) "neutral dynamics" the extinction time, i.e. the time reaching the absorbing state $N = 0$, scales linear in the initial system size $T \sim N_0$.

Finally, there are processes like the snowdrift game where the deterministic dynamics drives the population towards an interior fixed point well separated from the absorbing boundaries, $x = 0$ and $x = 1$. In such a case, starting from an initial state in the vicinity of the interior fixed point, the stochastic dynamics has to overcome a finite barrier in order to reach the absorbing state. This is similar to a chemical reaction with an activation barrier which is described by an Arrehnius law. Hence we expect that the extinction time scales exponentially in the initial population size $T \sim e^{N_0}$. This will be corroborated later by explicit calculations for the snowdrift game.

To summarize, the mean extinction time T can be used to classify evolutionary dynamics into a few fundamental regimes. For systems with a deterministic

[1] If instead of a linear birth-death process one would consider a symmetric random walk with hopping rate ϵ on a one-dimensional lattice with sites $x_i = ia$, the resulting equation would be a diffusion equation $\partial_t P(x,t) = D\partial_x^2 P(x,t)$ with diffusion constant $D = \epsilon a^2$. Restricting the random walk to a finite lattice with absorbing boundaries at $x_0 = 0$ and $x_N = Na := 1$ this would result in a diffusion constant scaling as the inverse square of the system size, $D \sim 1/N^2$. In the linear birth-death process, the corresponding amplitude D, measuring the magnitude of stochastic effects, scales as $D \sim 1/N$ since the rates are proportional to the size of the system; each individual has the same probability of undergoing a reaction.

drift towards the absorbing boundaries of states space, as frequently encountered in nonlinear dynamic systems with unstable interior fixed points, typical extinction times are expected to scale as $T \sim \ln N$. We refer to such a system as an "unstable" system. If, in contrast, the deterministic dynamics is characterized by a stable fixed point with some domain of attraction, we expect extinction times to scale as $T \sim e^N$. We will refer to those systems as "stable". The case of neutral dynamics yields $T \sim N$ and will be referred to as "neutral" (or marginally stable). There may also be intermediate scenarios with extinction times scaling as a power law in the population size, $T \sim N^\gamma$. Transitions between these regimes can occur and manifest as crossovers in the functional relation $T(N)$.

Recommended reading:

- *Introductory:* S.H. Strogatz, Nonlinear Dynamics and Chaos, Westview;
- *Advanced:* S. Wiggins, Introduction to Applied Nonlinear Dynamical Systems and Chaos, Springer.

Chapter 2

The May-Leonard model

Consider three subpopulations A, B and C which cyclically dominate each other. An individual of subpopulation A outperforms a B individual through "killing" (or "consuming"), symbolized by the ("chemical") reaction $AB \to A\oslash$, where $\oslash$ denotes an available empty space. In the same way, B outperforms C, and C beats A in turn, closing the cycle. We refer to these processes as selection and denote the corresponding rate by σ. To mimic a finite carrying capacity, we allow each subpopulation to reproduce only if an empty space is available, as described by the reaction $A\oslash \to AA$ and analogously for B and C. For all subpopulations, these reproduction events occur with rate μ, such that the three subpopulations equally compete for empty space. To summarize, the reactions that define the model (selection and reproduction) read

$$\begin{array}{llll} AB & \xrightarrow{\sigma} A\oslash\,, & A\oslash & \xrightarrow{\mu} AA\,, \\ BC & \xrightarrow{\sigma} B\oslash\,, & B\oslash & \xrightarrow{\mu} BB\,, \\ CA & \xrightarrow{\sigma} C\oslash\,, & C\oslash & \xrightarrow{\mu} CC\,. \end{array} \tag{2.1}$$

Let a, b, c denote the densities of subpopulations A, B, and C, respectively. The overall density ρ then reads $\rho = a + b + c$. As every lattice site is at most occupied by one individual, the overall density (as well as densities of each subpopulation) varies between 0 and 1, i.e. $0 \le \rho \le 1$. With these notations, the rate equations (RE) for the reaction (2.1) are given by

$$\begin{aligned} \partial_t a &= a[\mu(1-\rho) - \sigma c]\,, \\ \partial_t b &= b[\mu(1-\rho) - \sigma a]\,, \\ \partial_t c &= c[\mu(1-\rho) - \sigma b]\,. \end{aligned} \tag{2.2}$$

or in short

$$\partial_t \vec{a} = \vec{F}(\vec{a}) \tag{2.3}$$

These equations have been introduced and investigated by May and Leonard [1]. In the following, we discuss some of their properties. This will serve as an introduction to some of the standard tools on nonlinear dynamics: linear stability analysis, invariant manifolds, and normal forms.

The phase space of the model is organized by fixed point and invariant manifolds. Equations (2.2) possess four absorbing fixed points. One of these (unstable) is associated with the extinction of all subpopulations, $(a_1^*, b_1^*, c_1^*) =$

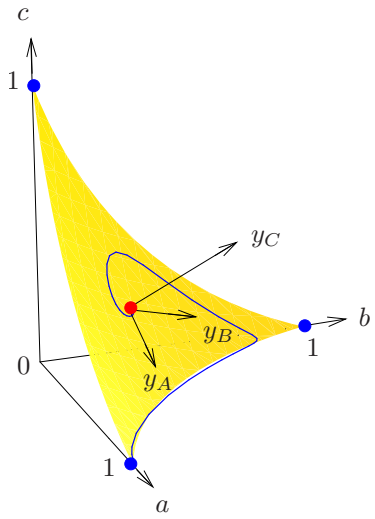

Figure 2.1: The phase space of the May-Leonard model. It is spanned by the densities a, b, and c of species A, B, and C. On an invariant manifold (yellow), the flows obtained as solutions of the rate equations (2.2) (an example is shown in blue) initially in the vicinity of the reactive fixed point (red) spiral outwards, approaching the heteroclinic cycle which connects three trivial fixed points (blue). In Subsection 2.2, we introduce the appropriate coordinates (y_A, y_B, y_C) which reveal the mathematical structure of the manifold and reflect the cyclic symmetry of the system.

$(0,0,0)$. The others are heteroclinic points (i.e. saddle points underlying the heteroclinic orbits) and correspond to the survival of only one subpopulation, $(a_2^*, b_2^*, c_2^*) = (1,0,0), (a_3^*, b_3^*, c_3^*) = (0,1,0)$ and $(a_4^*, b_4^*, c_4^*) = (1,0,0)$, shown in blue (dark gray) in Fig. 2.1. In addition, there exists a fixed point, indicated in red (gray) in Fig. 2.1, where all three subpopulations coexist (at equal densities), namely $(a^*, b^*, c^*) = \frac{\mu}{3\mu+\sigma}(1,1,1)$.

For a non-vanishing selection rate, $\sigma > 0$, Leonard and May [1] showed that the reactive fixed point is unstable, and the system asymptotically approaches the boundary of the phase space (given by the planes $a = 0$, $b = 0$, and $c = 0$). There, they observed *heteroclinic orbits*: the system oscillates between states where nearly only one subpopulation is present, with rapidly increasing cycle duration. While mathematically fascinating, this behavior was recognized to be unrealistic [1]. For instance, in a biological setting, the system will, due to finite-size fluctuations, always reach one of the absorbing fixed points in the vicinity of the heteroclinic orbit, and then only one population survives.

2.1 Linear stability analysis: Jordan normal form

Our goal is to study the nonlinear dynamics close to the coexistence (reactive) fixed point $\vec{a}^*$. We would like to know its stability and the typical behavior of a trajectory in its vicinity. To this end we introduce a shifted reference frame

by defining a displacement vector

$$\vec{x} = \vec{a} - \vec{a}^* = (a - a^*, b - b^*, c - c^*)^T \,. \tag{2.4}$$

Then

$$\partial_t \vec{x} = \vec{F}(\vec{x} + \vec{a}) = DF\mid_{\vec{a}*} \vec{x} + \vec{G}(\vec{x}) \tag{2.5}$$

where $A \equiv DF\mid_{\vec{a}*}$ is the Jacobian of $\vec{F}$ at the reactive fixed point $\vec{a}*$, and $\vec{G}(\vec{x})$ is the remaining nonlinear part of $\vec{F}(\vec{a} + \vec{a})$. From the structure of $\vec{F}$, we know that $\vec{G}$ is quadartic in x_A, x_B, and x_C. Explicitly one finds

$$A = -\frac{\mu}{3\mu + \sigma} \begin{pmatrix} \mu & \mu & \mu + \sigma \\ \mu + \sigma & \mu & \mu \\ \mu & \mu + \sigma & \mu \end{pmatrix} \,. \tag{2.6}$$

and

$$\vec{G} = \begin{pmatrix} \mu x_A(x_A + x_B) + x_A x_C(\mu + \sigma) \\ \mu x_B(x_B + x_C) + x_B x_A(\mu + \sigma) \\ \mu x_C(x_C + x_A) + x_C x_B(\mu + \sigma) \end{pmatrix} \,. \tag{2.7}$$

As the matrix A is circulant, its eigenvalues can be obtained from a particularly simple general formula (see e.g. [2]); they read:

$$\begin{aligned} \lambda_0 &= -\mu \,, \\ \lambda_\pm &= c_1 \pm i\omega \end{aligned} \tag{2.8}$$

with

$$\begin{aligned} c_1 &= \frac{1}{2} \frac{\mu\sigma}{3\mu + \sigma} \,, \\ \omega &= \frac{\sqrt{3}}{2} \frac{\mu\sigma}{3\mu + \sigma} \,. \end{aligned} \tag{2.9}$$

and corresponding (complex) eigenvectors ξ_0, and $\xi_\pm$; note that $\xi_0 = \frac{1}{3}(1, 1, 1)^T$ is easy to guess. This shows that the reactive fixed point is linearly stable along the eigendirection of the first eigenvalue λ_0. As elaborated below, there exists an invariant manifold [3] (including the reactive fixed point), that the system quickly approaches. To first order such a manifold is the plane normal to the eigendirection of λ_0. On this invariant manifold, flows spiral away from the reactive fixed point, which is an unstable spiral, as sketched in Fig. 2.1 (blue trajectory). [1]

[1] The linear stability analysis only reveals the local stability of the fixed points. The global instability of the reactive fixed point is proven by the existence of a Lyapunov function $\mathcal{L}$ [2, 1]:

$$\mathcal{L} = \frac{abc}{\rho^3} \,. \tag{2.10}$$

In fact, using Eqs. (2.2), the time derivative of $\mathcal{L}$ is found to be always non-positive,

$$\partial_t \mathcal{L} = -\frac{1}{2} \sigma \rho^{-4} abc\big[(a - b)^2 + (b - c)^2 + (c - a)^2\big] \leq 0 \,. \tag{2.11}$$

We note that $\partial_t \mathcal{L}$ vanishes only at the boundaries ($a = 0, b = 0$ or $c = 0$) and along the line of equal densities, $a = b = c$. The latter coincides with the eigendirection of λ_0, along which the system approaches the reactive fixed point. However, on the invariant manifold we recover $\partial_t \mathcal{L} < 0$, corresponding to a globally unstable reactive fixed point, as exemplified by the trajectory shown in Fig. 2.1.

To complete the linear stability analysis, it is useful to transform to Jordan normal form by introducing suitable coordinates (y_A, y_B, y_C) originating in the reactive fixed point. We choose the y_C-axis to coincide with the eigenvector of λ_0, and the coordinates y_A and y_B to span the plane normal to the axis y_C, forming an orthogonal set. The coordinates (y_A, y_B, y_C) are shown in Fig. 2.1. Such coordinates $\vec{y} = (y_A, y_B, y_C)$ are, e.g., obtained by the linear transformation $\vec{y} = \mathcal{S}\vec{x}$, with the matrix $\mathcal{S}$ given by

$$\mathcal{S} = \frac{1}{3}\begin{pmatrix} \sqrt{3} & 0 & -\sqrt{3} \\ -1 & 2 & -1 \\ 1 & 1 & 1 \end{pmatrix}, \tag{2.12}$$

To linear order this gives

$$\partial_t \vec{y} = J\vec{y} \tag{2.13}$$

with

$$J = SAS^{-1} = \begin{pmatrix} c_1 & \omega & 0 \\ -\omega & c_1 & 0 \\ 0 & 0 & -\mu \end{pmatrix} \tag{2.14}$$

With these results we may now rewrite the dynamics in the reference frame of the Jordan normal form which is the optimized frame for the linear stability analysis.

$$\partial_t \vec{y} = J\vec{y} + S\vec{G}(S^{-1}\vec{y}) \equiv J\vec{y} + \vec{H}(\vec{y}) \tag{2.15}$$

where one finds (with a straightforward calculation)

$$\vec{H}(\vec{y}) = \begin{pmatrix} \frac{\sqrt{3}}{4}\sigma\left[y_A^2 - y_B^2\right] - \frac{\sigma}{2}y_A y_B - \frac{1}{2}y_C\left[(6\mu+\sigma)y_A - \sqrt{3}\sigma y_B\right] \\ -\frac{\sigma}{4}\left[y_A^2 - y_B^2\right] - \frac{\sqrt{3}}{2}\sigma y_A y_B - \frac{1}{2}y_C\left[\sqrt{3}\sigma y_A + (6\mu+\sigma)y_B\right] \\ -(3\mu+\sigma)y_C^2 + \frac{\sigma}{4}\left[y_A^2 + y_B^2\right] \end{pmatrix} \tag{2.16}$$

As the RE (2.2) have one real eigenvalue smaller than zero and a pair of complex conjugate eigenvalues, they fall into the class of the Poincaré-Andronov-Hopf bifurcation, well known in the mathematical literature [3]. The theory of invariant and center manifolds allows us to recast these equations into a normal form. The latter, as discussed in the next section, will turn out to be extremely useful in the derivation of the CGLE. In the following, we derive the invariant manifold to second order as well as the normal form of the RE.

2.2 Invariant manifold

An invariant manifold is a subspace, embedded in the phase space, which is left invariant by the RE, Eq.(2.2), i.e. by the deterministic dynamics. In the phase space, this means that flows starting on an invariant manifold always lie and evolve on it. Here, we consider a two-dimensional invariant manifold M associated with the reactive fixed point of the RE (2.2) onto which all trajectories (initially away from the invariant manifold) decay exponentially quickly. We call this manifold M the *reactive manifold*. Upon restricting the dynamics to that reactive invariant manifold, the system's degrees of freedom are reduced from three to two, which greatly simplifies the mathematical analysis.

To determine this invariant manifold, we notice that the eigenvector of the eigenvalue $\lambda_0 < 0$ at the reactive fixed point is a stable (attractive) direction.

Therefore, to lowest order around the reactive fixed point, the invariant manifold is simply the plane normal to the eigendirection of λ_0. To parameterize the invariant manifold sketched in Fig. 2.1, we seek a function $M(y_A, y_B)$, with $y_C = M(y_A, y_B)$. If all nonlinearities of the RE are taken into account, this is a very complicated problem. However, for our purpose it is sufficient to expand M to second order in y_A, y_B. As the invariant manifold is left invariant by the RE, by definition, M must obey

$$\partial_t M\big(y_A(t), y_B(t)\big) = \frac{\partial M}{\partial y_A}\partial_t y_A + \frac{\partial M}{\partial y_B}\partial_t y_B = \partial_t y_C\Big|_{y_C=M} . \tag{2.17}$$

To linear order in y_A and y_B, we simply have $M = 0$ and recover $y_C = 0$, corresponding to the plane normal to the y_C-direction. We have anticipated this result above: to first order, the invariant manifold coincides with this plane, and is tangential to it when higher orders are included. To second order, only linear terms of $\partial_t y_A, \partial_t y_B$ contribute to Eq. (2.17). The latter are invariant under rotations in the (y_A, y_B)-plane, and M must obey the same symmetry. It is therefore proportional to $y_A^2 + y_B^2$. After some simple calculations, one obtains:

$$y_C = M(y_A, y_B) = \frac{\sigma}{4\mu}\frac{3\mu+\sigma}{3\mu+2\sigma}(y_A^2 + y_B^2) + o(\vec{y}^2) . \tag{2.18}$$

The comparison of this expression for the invariant manifold, valid to second order, with the numerical solutions of the RE (2.2) (which should, up to an initial transient, lie on the invariant manifold) confirms that (2.18) is an accurate approximation, with only minor deviations occurring near the boundaries of the phase space.

2.3 Normal form

Nonlinear systems are notably characterized by the bifurcations that they exhibit [3]. Normal forms are defined as the simplest differential equations that capture the essential features of a system near a bifurcation point, and therefore provide insight into the system's universal behavior. Here, we derive the normal form associated with the RE (2.2) of the May-Leonard model and show that they belong to the universality class of the Hopf bifurcation [3]. Below, we demonstrate that this property allows to describe the system in terms of a well-defined complex Ginzburg-Landau equation.

Restricting the (deterministic) dynamics onto the invariant manifold, given by Eq. (2.18), the system's behavior can be analyzed in terms of two variables. Here, we choose to express y_C as a function of y_A and y_B, with the resulting rate equations (up to cubic oder) given up to third order by:

$$\begin{aligned}
\partial_t y_A &= \frac{\mu\sigma}{2(3\mu+\sigma)}\big[y_A + \sqrt{3}y_B\big] + \frac{\sqrt{3}}{4}\sigma\big[y_A^2 - y_B^2\big] - \frac{\sigma}{2}y_A y_B \\
&- \frac{\sigma(3\mu+\sigma)}{8\mu(3\mu+2\sigma)}\big(y_A^2 + y_B^2\big)\big[(6\mu+\sigma)y_A - \sqrt{3}\sigma y_B\big] + o(y^3) , \\
\partial_t y_B &= \frac{\mu\sigma}{2(3\mu+\sigma)}\big[y_B - \sqrt{3}y_A\big] - \frac{\sigma}{4}\big[y_A^2 - y_B^2\big] - \frac{\sqrt{3}}{2}\sigma y_A y_B \\
&- \frac{\sigma(3\mu+\sigma)}{8\mu(3\mu+2\sigma}\big(y_A^2 + y_B^2\big)\big[\sqrt{3}\sigma y_A + (6\mu+\sigma)y_B\big] + o(y^3) .
\end{aligned} \tag{2.19}$$

This set of nonlinear equations can be cast into a normal form (see [3] Chapter 2.2) by performing a nonlinear variable transformation $\vec{y} \to \vec{z}$ which eliminates the quadratic terms and preserves the linear ones (i.e. $\vec{y}$ and $\vec{z}$ coincide to linear order). As an Ansatz for such a transformation, we choose the most general quadratic expression in $\vec{y}$ for the new variable $\vec{z}$. [2] One finds for the normal form of the RE in the new variables:

$$\begin{aligned} \partial_t z_A &= c_1 z_A + \omega z_B - c_2\big(z_A + c_3 z_B\big)(z_A^2 + z_B^2) + o(\vec{z}^3)\,, \\ \partial_t z_B &= c_1 z_B - \omega z_A - c_2\big(z_B - c_3 z_A\big)(z_A^2 + z_B^2) + o(\vec{z}^3)\,. \end{aligned} \tag{2.22}$$

In these equations,

$$\omega = \frac{\sqrt{3}}{2}\frac{\mu\sigma}{3\mu+\sigma}\,, \tag{2.23}$$

is the (linear) frequency of oscillations around the reactive fixed point. The constant

$$c_1 = \frac{1}{2}\frac{\mu\sigma}{3\mu+\sigma}\,, \tag{2.24}$$

gives the intensity of the linear drift away from the fixed point, while

$$c_2 = \frac{\sigma(3\mu+\sigma)(48\mu+11\sigma)}{56\mu(3\mu+2\sigma)}\,, \tag{2.25}$$

$$c_3 = \frac{\sqrt{3}(18\mu+5\sigma)}{48\mu+11\sigma}\,, \tag{2.26}$$

are the coefficients of the cubic corrections. In complex notation, $z = z_A + i z_B$, we have

$$\partial_t z = (c_1 - i\omega)z - c_2\big(1 + i c_3\big)\mid z\mid^2 z\,. \tag{2.27}$$

To gain some insight into the dynamics in the normal form, it is useful to rewrite (2.22) in polar coordinates (r,ϕ), where $z_A = r\cos\phi, z_B = r\sin\phi$. This leads to

$$\begin{aligned} \partial_t r &= r[c_1 - c_2 r^2]\,, \\ \partial_t \theta &= -\omega + c_2 c_3 r^2\,. \end{aligned} \tag{2.28}$$

[2] The equations of motion (2.19) comprise quadratic and cubic terms. To recast Eqs. (2.19) in their normal form, we seek a transformation allowing to eliminate the quadratic terms. We make the Ansatz of a quadratic transformation $\vec{y} \to \vec{z}$ and determine the coefficients by cancelling the quadratic contributions to the RE in the $\vec{z}$ variables, this leads to

$$\begin{aligned} z_A &= y_A + \frac{3\mu+\sigma}{28\mu}[\sqrt{3}y_A^2 + 10 y_A y_B - \sqrt{3}y_B^2]\,, \\ z_B &= y_B + \frac{3\mu+\sigma}{28\mu}[5y_A^2 - 2\sqrt{3}y_A y_B - 5y_B^2]\,. \end{aligned} \tag{2.20}$$

To second order, this nonlinear transformation can be inverted:

$$\begin{aligned} y_A &= z_A - \frac{3\mu+\sigma}{28\mu}[\sqrt{3}z_A^2 + 10 z_A z_B - \sqrt{3}z_B^2] + \frac{(3\mu+\sigma)^2}{14\mu^2}[z_A^3 + z_A z_B^2] + o(z^3)\,, \\ y_B &= z_B - \frac{3\mu+\sigma}{28\mu}[5z_A^2 - 2\sqrt{3}z_A z_B - 5z_B^2] + \frac{(3\mu+\sigma)^2}{14\mu^2}[z_A^2 z_B + z_B^3] + o(z^3)\,. \end{aligned} \tag{2.21}$$

With these expressions, one can check that equations of motion (2.19) are recast in the normal form (2.22).

These equations only have a radial dependence, which clearly reveals a polar symmetry. They predict the emergence of a limit cycle of radius $r = \sqrt{c_1/c_2}$ and therefore fall into the universality class of the (supercritical) Hopf bifurcation. However, when all nonlinearities are taken into account, the RE (2.2) give rise to heteroclinic orbits instead of limit cycles. The latter rapidly approach the boundaries of the phase space, and thus are in general well separated from the limit cycles predicted by (2.28). When comparing results inferred from the CGLE and stochastic lattice simulations in the results section, we have shown how this causes some quantitative mismatch, stemming from the differences between the solutions of (2.2) and (2.28). However, we have also seen that most features of the system are actually aptly captured by the normal form (2.22). Elsewhere, it will be shown that mutations between subpopulations lead to limit cycles resulting from a Hopf bifurcation.

Recommended reading:

- P. Glendinning, "Stability, Instability and Chaos", Cambridge University Press.
- S. Wiggins, Introduction to Applied Nonlinear Dynamical Systems and Chaos, Springer.

Chapter 3

Spatial Games with Cyclic Dominance

In this chapter we analyze the stochastic spatially-extended version of the May-Leonard model [1]. We adopt an interacting particle description where individuals of all subpopulations are arranged on a lattice. Denote L the linear size of the d-dimensional hypercubic lattice (i.e. the number of sites along one edge), such that the total number of sites reads $N = L^d$. In this approach, each site of the grid is either occupied by one individual or empty, meaning that the system has a finite carrying capacity, and the reactions (see Fig.3.1) are then only allowed between *nearest neighbors*. In addition, we endow the individuals with a certain form of mobility. Namely, at rate ϵ all individuals can exchange their position with a nearest neighbor. With that same rate ϵ, any individual can also hop on a neighboring empty site. These exchange processes lead to an effective diffusion of the individuals described by a diffusion constant D.

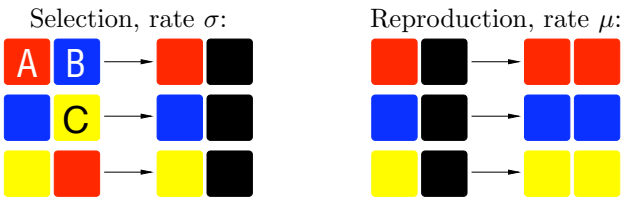

Figure 3.1: Individuals on neighboring sites may react with each other according to the rules of cyclic dominance (selection), or individuals may give birth to new individuals if they happen to be next to an empty site (reproduction).

The goal of this chapter is to analyze the spatio-temporal dynamics at asymptotically long time scales as a function of the hopping and reaction rates. We will learn that the mobility of the individuals, characterized in terms of their diffusion constant, has a critical influence on species diversity. When mobility exceeds a certain value, biodiversity is jeopardized and lost. In contrast, below this critical threshold all subpopulations coexist and the spatial stochastic model of cyclically interacting subpopulations self-organizes into regular, geometric spiral waves. The latter become visible on the scale of a large number

of interacting individuals, see Fig. 3.2 (right). In contrast, stochastic effects solely dominate on the scale of a few individuals, see Fig. 3.2 (left), which interact locally with their nearest neighbors. Spatial separation of subpopulations starts to form on an intermediate scale, Fig. 3.2 (middle), where mobility leads to fuzzy domain boundaries, with major contributions of noise. On a larger scale, Fig. 3.2 (right), these fuzzy patterns adopt regular geometric shapes. As shown below, the latter are jointly determined by the deterministic dynamics and intrinsic stochastic effects.

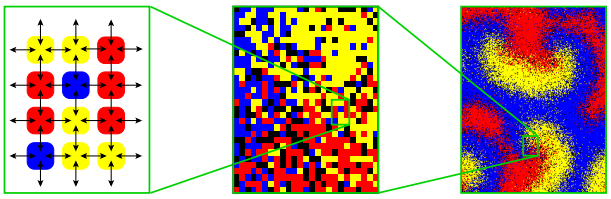

Figure 3.2: The stochastic spatial system at different scales. Here, each of the colors yellow, red, and blue (level of gray) represents one species, and black dots identify empty spots. Left: Individuals are arranged on a spatial lattice and randomly interact with their nearest neighbors. Middle: At the scale of about 1,000 individuals, stochastic effects dominate the system's appearance, although domains dominated by different subpopulations can already be detected. Right: About 50,000 mobile interacting individuals self-organize into surprisingly regular spiral waves.

In the following, we elucidate this subtle interplay between noise and space by mapping - in the continuum limit - the stochastic spatial dynamics onto a set of *stochastic partial differential equations* (SPDE) and, using tools of dynamical systems (such as normal forms and invariant manifolds), by recasting the underlying deterministic kinetics in the form of a *complex Ginzburg-Landau equation* (CGLE). The CGLE allows us to make analytical predictions for the spreading velocity and wavelength of the emerging spirals waves.

3.1 Simulation results for the lattice gas model

We start with a description of the results obtained from stochastic simulations of the lattice gas model. Typical snapshots of the steady states are shown in Fig. 3.3 [1]. When the mobility of the individuals is low, one finds that all species coexist and self-arrange by forming patterns of moving spirals. Increasing the mobility D, these structures grow in size, and disappear for large enough D. In the absence of spirals, the system adopts a uniform state where only one species is present, while the others have died out. Which species remains is subject to a random process, all species having equal chances to survive in the symmetric model defined above.

The transition from the reactive state containing spirals to the absorbing state with only one subpopulation left is a non-equilibrium phase transition.

[1] You may also want to have a look at the movies posted on `http://www.theorie.physik.uni-muenchen.de/lsfrey/research/fields/biological_physics/2007_004/`. There is also a Wolfram demonstration project which you can download from the web: `http://demonstrations.wolfram.com/BiodiversityInSpatialRockPaperScissorsGames/`.

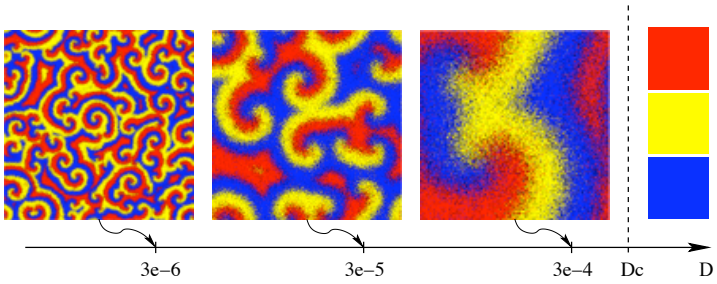

Figure 3.3: Snapshots obtained from lattice simulations are shown of typical states of the system after long temporal development (i.e. at time $t \sim N$) and for different values of D (each color, blue, yellow and red, represents one of the species and black dots indicate empty spots). Increasing D (from left to right), the spiral structures grow, and outgrow the system size at the critical mobility D_c: then, coexistence of all three species is lost and uniform populations remain (right).

One way to characterize the transition is to ask how the extinction time T, i.e. the time for the system to reach one of its absorbing states, scales with system size N. In our analysis of the role of stochasticity in the Introduction we have found the following classification scheme. If $T \sim N$, the stability of coexistence is marginal. Conversely, longer (shorter) waiting times scaling with higher (lower) powers of N indicate stable (unstable) coexistence. These three scenarios can be distinguished by computing the probability $P_{\rm ext}$ that two species have gone extinct after a waiting time $t \sim N$. In Fig. 3.4, the dependence of $P_{\rm ext}$ on the mobility D is shown for different system sizes. For illustration, we have considered equal reaction rates for selection and reproduction, and, without loss of generality, set the time-unit by fixing $\sigma = \mu = 1$. Increasing the system size

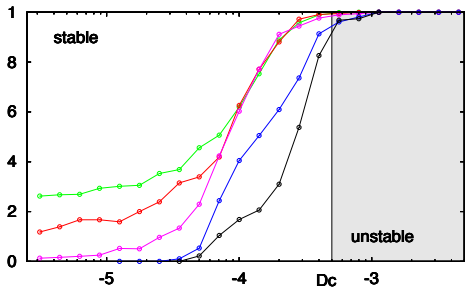

Figure 3.4: The extinction probability $P_{\rm ext}$ that, starting with randomly distributed individuals on a square lattice, the system has reached an absorbing state after a waiting time $t \sim N$. $P_{\rm ext}$ is shown as function of the mobility D (and $\sigma = \mu = 1$) for different system sizes: $N = 20 \times 20$ (green), $N = 30 \times 30$ (red), $N = 40 \times 40$ (purple), $N = 100 \times 100$ (blue), and $N = 200 \times 200$ (black). As the system size increases, the transition from stable coexistence ($P_{\rm ext} = 0$) to extinction ($P_{\rm ext} = 1$) sharpens at a critical mobility $D_c \approx (4.5 \pm 0.5) \times 10^{-4}$. Figure taken from Ref.[4]

N, a sharpened transition emerges at a critical value $D_c = (4.5 \pm 0.5) \times 10^{-4}$ for the fraction of the entire lattice area explored by an individual in one time-unit. Below D_c, the extinction probability P_{ext} tends to zero as the system size increases, and coexistence is stable. In contrast, above the critical mobility, the extinction probability approaches one for large system size, and coexistence is unstable.

As a central result one finds that there exists a critical value D_c such that a low mobility $D < D_c$ guarantees coexistence of all three species, while $D > D_c$ induces extinction of two of them, leaving a uniform state with only one species.

3.2 Reaction-diffusion equations

Before embarking into the endeavor of fully analyzing the non-equilibrium dynamics let us disregard for the moment the effect of noise and consider the deterministic spatial dynamics. We consider a continuum limit where the linear dimension of the lattice is chosen as the basic length unit, $L \equiv 1$, and hence the lattice constant becomes $a = 1/N^{1/d}$. Then the ensuing diffusion-reaction equations for the density vector $\vec{a}(\vec{r},t) = (a(\vec{r},t), b(\vec{r},t), c(\vec{r},t))$ reads

$$\partial_t \vec{a}(\vec{r},t) = D\nabla^2 \vec{a} + \vec{F}(\vec{a}) \tag{3.1}$$

with the macroscopic diffusion constant

$$D = \frac{\epsilon}{dN^{2/d}} \qquad \left(d = 2: \; D = \frac{\epsilon}{2N}\right) . \tag{3.2}$$

We are interested in the limit $N \to \infty$ and want the macroscopic diffusion constant D to be finite in that limit. This implies that the rate ϵ becomes large compared to the selection and reproduction rates, μ and σ, and thus - in the lattice model - a large number of hopping and exchange events occurs between two reactions.

Upon employing the results of the nonlinear dynamics we may project those reaction-diffusion equations onto the *reactive manifold* M, and obtain:

$$\partial_t z \;\; = \;\; D\nabla^2 z + (c_1 - i\omega)z - c_2(1 + ic_3)|z|^2 z \, . \tag{3.3}$$

Here, we recognize the celebrated *complex Ginzburg-Landau equation* (CGLE), whose properties have been extensively studied [5, 6]. In particular, it is known that in two dimensions the latter gives rise to a broad range of coherent structures, including spiral waves whose velocity, wavelength and frequency can be computed analytically.

3.2.1 The linear spreading velocity

In the stochastic simulations we have found that in the long-time regime the system exhibits traveling waves. In the steady state, regions with nearly only A individuals are invaded by a front of C individuals, which is taken over by B in turn, and so on. This can be understood as a *front propagation phenomenon* into an unstable state as follows. The complex Ginzburg-Landau equation has an unstable fixed point at the reactive center, $z = 0$. Hence any small perturbation will grow and lead to a spreading pulse whose form is determined by the

nonlinearities in the equation. Its velocity, however, can already be calculated by analyzing the linearized equations; for a recent review on the theory of front propagation into unstable states see Ref.[7].

The CGLE (3.3) linearized around the coexistence state $z = 0$ reads

$$\partial_t z(\vec{r}, t) = D\Delta z(\vec{r}, t) + (c_1 - i\omega)z(\vec{r}, t) \tag{3.4}$$

We perform a Fourier transformation

$$\tilde{z}(\vec{k}, t) = \int_{-\infty}^{\infty} d\vec{r}\; z(\vec{r}, t)e^{-i\vec{k}\cdot\vec{r}}\;, \tag{3.5}$$

and make the Ansatz

$$\tilde{z}(\vec{k}, t) = \bar{z}(\vec{k})\, e^{-i\Omega(\vec{k})t} \tag{3.6}$$

for each Fourier mode. The linearized CGLE then give the following dispersion relation

$$\Omega(k) = \omega + i(c_1 - Dk^2)\;, \tag{3.7}$$

where $k = |\vec{k}|$. As $\mathrm{Im}\,\Omega(k) > 0$ for $k^2 < c_1/D$, the state $z = 0$ is linearly unstable in this range of wavevectors k. This confirms the analysis of the spatially homogeneous nonlinear dynamics (2.2), where we already found that the coexistence fixed point is unstable. As for other systems characterized by fronts propagating into unstable states [7], from Eq. (3.4) one can now compute the linear spreading velocity, i.e. the speed v^* at which fronts (e.g. generated by local perturbations around $z = 0$) propagate. For completeness, we repeat the classical treatment which can, e.g., be found in [7]. A Fourier back-transform of the above results gives

$$z(\vec{x}, t) = \int \frac{d^2k}{(2\pi)^2}\, \bar{z}(\vec{k})\, e^{i\vec{k}\cdot\vec{x} - i\Omega(\vec{k})t} \tag{3.8}$$

Say the front is propagating with a speed $\vec{v}^* = v^*\hat{e}_x$ in the x-direction. Then in the co-moving frame, $\vec{\xi} = \vec{x} - \vec{v}^*t$, this velocity is determined (self-consistently) such that the ensuing expression of the pulse form does neither grow nor decay

$$z(\vec{\xi}, t) = \int \frac{d^2k}{(2\pi)^2}\, \bar{z}(\vec{k})\, e^{i\vec{k}\cdot\vec{\xi} - i[\Omega(\vec{k}) - \vec{v}^*\cdot\vec{k}]t} \tag{3.9}$$

For large times, $t \to \infty$, the integral may be performed by a saddle-point expansion with the saddle k^* determined by

$$\frac{d[\Omega(k) - v^*k]}{dk}\;|_{k^*} = 0 \quad \Rightarrow v^* = \frac{d\Omega(k)}{dk}\;|_{k^*} \tag{3.10}$$

and the integral given to leading order by

$$z(\vec{\xi}, t) \propto e^{i\vec{k}\cdot\vec{\xi} - i[\Omega(k^*) - \vec{v}^*\cdot\vec{k}]t} \tag{3.11}$$

In order for this to neither grow or decay we must have

$$\mathrm{Im}\,\Omega(k_*) - v^*\mathrm{Im}\,k_* = 0 \quad \Rightarrow v^* = \frac{\mathrm{Im}\,\Omega(k_*)}{\mathrm{Im}\,k_*} \tag{3.12}$$

Hence the linear spreading velocity is obtained by determining a wavevector k_* according to

$$\left.\frac{d\Omega(k)}{dk}\right|_{k_*} = \frac{\mathrm{Im}\,\Omega(k_*)}{\mathrm{Im}\,k_*} \equiv v^* \ . \tag{3.13}$$

The first equality singles out k_* and the second defines the linear spreading velocity v^*. Here, one finds:

$$\mathrm{Re}\,k_* = 0 \ , \quad \mathrm{Im}\,k_* = \sqrt{c_1/D} \ , \tag{3.14}$$

and

$$v^* = 2\sqrt{c_1 D} = 2\sqrt{D}\,\sqrt{\frac{1}{2}\frac{\mu\sigma}{3\mu+\sigma}} \, . \tag{3.15}$$

3.2.2 Wavelength and frequency

To determine analytically the wavelength λ and the frequency Ω of the spiral waves, the (cubic) nonlinear terms of the CGLE (3.3) have to be taken into account. From the understanding gained in the previous sections, we make a traveling-wave ansatz $z(\vec{r},t) = Ze^{-i\Omega t - i\vec{k}\cdot\vec{r}}$ leading to the following dispersion relation (with $k = |\vec{k}|$)

$$\Omega(k) = \omega + i(c_1 - Dk^2) - c_2(i + c_3)Z^2 \, . \tag{3.16}$$

Separating real and imaginary parts, we can solve for Z, resulting in $Z^2 = (c_1 - Dk^2)/c_2$. As already found above, the range of wavevectors that yield traveling wave solutions is therefore given by $k < \sqrt{c_1/D}$. The dispersion relation can, upon eliminating Z, be rewritten as

$$\Omega(k) = \omega + c_3(Dk^2 - c_1). \tag{3.17}$$

As manifests on the RHS of (3.17), Ω comprises two contributions. On the one hand there is ω, acting as a "background frequency", which stems from the nonlinear nature of the dynamics and is already accounted by (2.2) when the system is spatially homogeneous. On the other hand, the second contribution on the RHS of (3.17) is due to the spatially-extended character of the model and to the fact that traveling fronts propagate with velocity v^*, therefore generating oscillations with a frequency of v^*k. Both contributions superpose and, to sustain a velocity v^*, the dynamics selects a wavenumber k^{sel} according to the relation $\Omega(k^{\mathrm{sel}}) = \omega + v^*k^{\mathrm{sel}}$ [7]. Solving this equation for k^{sel} under the restriction $k^{\mathrm{sel}} < \sqrt{c_1/D}$ yields

$$k^{\mathrm{sel}} = \frac{\sqrt{c_1}}{c_3\sqrt{D}}\left(1 - \sqrt{1+c_3^2}\right) \, . \tag{3.18}$$

Analytical expressions of the frequency $\Omega(k^{\mathrm{sel}})$ and of the wavelength of the spirals, $\lambda = 2\pi/k^{\mathrm{sel}}$, can be obtained immediately from (3.17) and (3.18). In fact, the frequency reads

$$\Omega = \Omega(q^{\mathrm{sel}}) = \omega + \frac{2c_1}{c_3}\left(1 - \sqrt{1+c_3^2}\right) \, , \tag{3.19}$$

and the wavelength is given by

$$\lambda = \frac{2\pi c_3 \sqrt{D}}{\sqrt{c_1}\left(1 - \sqrt{1 + c_3^2}\right)} \,. \tag{3.20}$$

The expressions (3.18)-(3.20) have been derived by considering a traveling wave ansatz as described above. The latter hold in *arbitrary dimensions*. However, while traveling waves appear in one dimensions, in higher dimensions, the generic emerging structures are somewhat different. E.g. rotating spirals arise in two dimensions, as described in this article, while scroll waves are robust solutions of the CGLE (3.3) in three spatial dimensions [6]. However, the characteristic properties of these patterns, such as wavelength and frequency, still agree with those of traveling waves. Indeed, concerning the dynamical system investigated in this article, we have shown how the self-forming spirals are well characterized by the expressions (3.19) and (3.20). The same system studied in three dimensions is therefore expected to exhibit an entanglement of scroll waves, whose wavelengths and frequencies are again given by Eqs. (3.19) and (3.20).

As will become clear later, these results for the spreading velocity and the wavelength actually remain valid even in the presence of noise!

3.3 The role of noise

There is noise in the system due to the stochastic nature of all processes and the discrete character of the individuals. It plays an important role for the system's dynamics. In particular - as we will see - it is responsible for the non-equilibrium phase transition from the reactive state into one of the absorbing states.

The way one can deal with the noise depends on the expected stationary state! If the stationary state contains many individuals of each species (a macroscopic number) one may perform a Kramers-Moyal expansion (*low noise limit*). If, however, the stationary state is some kind of absorbing state where all fluctuations have died out, a different approach is called for. Then one has to employ a Fock space formulation to map the dynamics of the master equation to a path integral measure with an appropriate action $\mathcal{S}$ (Doi-Peliti formalism). From this action one may then derive a Langevin equation for a set of complex density fields whose averages and correlation functions characterize the dynamics towards the absorbing state (*strong noise limit*). Though both of these approaches look superficially the same, they are fundamentally different. In a low-noise approximation the noise always turns out to be real but it becomes a complex (imaginary) quantity in the strong noise limit!

Here, we restrict ourselves to the behavior of the system in the reactive state where we can use a *low noise approximation* to find the appropriate *noisy diffusion-reaction equation*. We consider large system sizes N where a stochastic description in terms of Fokker-Planck equations is generally appropriate [8, 9]. The latter can be obtained from Kramers-Moyal expansion (i.e. a system-size expansion) of the underlying master equation. In Fokker-Planck equations, fluctuations are encoded in a noise matrix denoted $\mathcal{B}$. Equivalently, a set of Ito stochastic (partial) differential equations (often referred to as Langevin equations) can be systematically derived. For these stochastic partial differential

equations (SPDE), the noise, often white, is encoded in the "square root" of the matrix $\mathcal{B}$. Namely, in this framework, the strength of fluctuations and the correlations are given by a matrix $\mathcal{C}$, defined as $\mathcal{C}\mathcal{C}^T = \mathcal{B}$. Below, we derive the relevant contributions to the noise matrices $\mathcal{B}$ and $\mathcal{C}$, which lead to the appropriate stochastic partial differential equations (SPDE) of the system.

As discussed in the next two subsections, the noise resulting from the reaction terms dominates by a factor $\sqrt{N}$ over the noise originating from hopping, and we find the following set of stochastic nonlinear differential equations

$$\partial_t a(\vec{r},t) = D\Delta a(\vec{r},t) + \mathcal{A}_A[\vec{a}] + \mathcal{C}_A[\vec{a}]\xi_A\,, \tag{3.21}$$
$$\partial_t b(\vec{r},t) = D\Delta b(\vec{r},t) + \mathcal{A}_B[\vec{a}] + \mathcal{C}_B[\vec{a}]\xi_B\,, \tag{3.22}$$
$$\partial_t c(\vec{r},t) = D\Delta c(\vec{r},t) + \mathcal{A}_C[\vec{a}] + \mathcal{C}_C[\vec{a}]\xi_C\,, \tag{3.23}$$

or in short

$$\partial_t \vec{a}(\vec{r},t) = D\Delta\vec{a}(\vec{r},t) + \mathcal{A}[\vec{a}] + \mathcal{C}[\vec{a}]\cdot\vec{\xi} \tag{3.24}$$

where Δ denotes the Laplacian operator, and the Gaussian white noise terms $\xi_i(\vec{r},t)$ have a spatio-temporal dependence, with the correlations

$$\langle \xi_i(\vec{r},t)\xi_j(\vec{r}',t')\rangle = \delta_{ij}\delta(\vec{r}-\vec{r}')\delta(t-t')\,. \tag{3.25}$$

and

$$\mathcal{C}_A = \frac{1}{\sqrt{N}}\sqrt{a(\vec{r},t)\big[\mu(1-\rho(\vec{r},t)) + \sigma c(\vec{r},t)\big]}\,,$$
$$\mathcal{C}_B = \frac{1}{\sqrt{N}}\sqrt{b(\vec{r},t)\big[\mu(1-\rho(\vec{r},t)) + \sigma a(\vec{r},t)\big]}\,,$$
$$\mathcal{C}_C = \frac{1}{\sqrt{N}}\sqrt{c(\vec{r},t)\big[\mu(1-\rho(\vec{r},t)) + \sigma b(\vec{r},t)\big]}\,. \tag{3.26}$$

Note that the reaction term derived in the Kramers-Moyal expansion is identical - as it must - to the corresponding nonlinear drift term in the diffusion-reaction equation, $\vec{F}[\vec{a}] = \mathcal{A}[\vec{a}]$.

3.3.1 Kramers-Moyal expansion of the reaction terms

Since noise terms stemming from the reactions (2.1) are local, they may be derived considering the stochastic non-spatial system, i.e. the well-mixed system. Denotind $\vec{a} = (a,b,c)$ the frequencies of the three subpopulations A, B, and C, the Master equation for the time-evolution of the probability $P(\vec{a},t)$ of finding the system in state $\vec{a}$ at time t reads

$$\partial_t P(\vec{a},t) = \sum_{\delta\vec{a}}\Big[P(\vec{a}+\delta\vec{a},t)\mathcal{W}_{\vec{a}+\delta\vec{a}\to\vec{a}} - P(\vec{a},t)\mathcal{W}_{\vec{a}\to\vec{a}+\delta\vec{a}}\Big]\,. \tag{3.27}$$

Hereby, $\mathcal{W}_{\vec{a}\to\vec{a}+\delta\vec{a}}$ denotes the transition probability from state $\vec{a}$ to the state $\vec{a}+\delta\vec{a}$ within one time step; summation extends over all possible changes $\delta\vec{a}$. The relevant changes $\delta\vec{a}$ in the densities result from the basic reactions (2.1); as an example, concerning the change in the density of the subpopulation A, it reads $\delta a = 1/N$ in the reaction $A\oslash \xrightarrow{\mu} AA$, $\delta a = -1/N$ in the reaction $CA \xrightarrow{\sigma} C\oslash$, and zero in the remaining ones. Concerning the rates for these reactions, we

choose the unit of time such that, on average, every individual reacts once per time step. The transition rates resulting from the reactions (2.1) then read $\mathcal{W} = N\sigma ac$ for the reaction $CA \xrightarrow{\sigma} C\oslash$ and $\mathcal{W} = N\mu a(1-a-b-c)$ for $A\oslash \xrightarrow{\mu} AA$. Transition probabilities associated with all other reactions (2.1) follow analogously.

The Kramers-Moyal expansion [10] of the Master equation is an expansion in the increment $\delta\vec{a}$, which is proportional to N^{-1}. Therefore, it may be understood as an expansion in the inverse system size N^{-1}. To second order in $\delta\vec{a}$, it yields the (generic) Fokker-Planck equation [10]:

$$\partial_t P(\vec{a},t) = -\partial_i[\mathcal{A}_i(\vec{a})P(\vec{a},t)] + \frac{1}{2}\partial_i\partial_j[\mathcal{B}_{ij}(\vec{a})P(\vec{a},t)] \,. \tag{3.28}$$

Hereby, the summation convention implies sums carried over the indices $i,j \in \{A,B,C\}$. According to the Kramers-Moyal expansion, the quantities $\mathcal{A}_i$ and $\mathcal{B}_{ij}$ read [10]

$$\begin{aligned}\mathcal{A}_i(\vec{a}) &= \sum_{\delta\vec{a}} \delta s_i \mathcal{W}(\vec{a}\to\vec{a}+\delta\vec{a}) \,,\\ \mathcal{B}_{ij}(\vec{a}) &= \sum_{\delta\vec{a}} \delta s_i \delta s_j \mathcal{W}(\vec{a}\to\vec{a}+\delta\vec{a}) \,.\end{aligned} \tag{3.29}$$

Note that $\mathcal{B}$ is symmetric.

As an example, we now present the calculation of $\mathcal{A}_A(\vec{a})$. The relevant changes δa result from the reactions $A\oslash \xrightarrow{\mu} AA$ and $CA \xrightarrow{\sigma} C\oslash$. The corresponding rates as well as the changes in the density of subpopulation A have been given above; together, we obtain $\mathcal{A}_A(\vec{a}) = \mu a(1-a-b-c) - \sigma ac$. The other quantities are computed analogously; eventually, one finds

$$\begin{aligned}\mathcal{A}_A(\vec{a}) &= \mu a(1-a-b-c) - \sigma ac \,,\\ \mathcal{A}_B(\vec{a}) &= \mu b(1-a-b-c) - \sigma ab \,,\\ \mathcal{A}_C(\vec{a}) &= \mu c(1-a-b-c) - \sigma bc \,,\end{aligned} \tag{3.30}$$

and

$$\begin{aligned}\mathcal{B}_{AA}(\vec{a}) &= N^{-1}\left[\mu a(1-a-b-c) + \sigma ac\right] \,,\\ \mathcal{B}_{BB}(\vec{a}) &= N^{-1}\left[\mu b(1-a-b-c) + \sigma ab\right] \,,\\ \mathcal{B}_{CC}(\vec{a}) &= N^{-1}\left[\mu c(1-a-b-c) + \sigma bc\right] \,.\end{aligned} \tag{3.31}$$

The well-known correspondence between Fokker-Planck equations and Ito calculus [9] implies that (3.28) is equivalent to the following set of Ito stochastic differential equations:

$$\begin{aligned}\partial_t a &= \mathcal{A}_A + \mathcal{C}_{AA}\xi_A \,,\\ \partial_t b &= \mathcal{A}_B + \mathcal{C}_{BB}\xi_B \,,\\ \partial_t c &= \mathcal{A}_C + \mathcal{C}_{CC}\xi_C \,.\end{aligned} \tag{3.32}$$

Hereby, the ξ_i denotes (uncorrelated) Gaussian white noise terms. The matrix $\mathcal{C}$ is defined from $\mathcal{B}$ via the relation $\mathcal{C}\mathcal{C}^T = \mathcal{B}$ [9]. As $\mathcal{B}$ is diagonal, we may choose $\mathcal{C}$ diagonal as well, with the square roots of the corresponding diagonal entries of $\mathcal{B}$ on the diagonal.

3.3.2 Kramers-Moyal expansion of the diffusion term

Diffusion couples two nearest neighboring lattice sites $\vec{r}$ and $\vec{r}'$. The rate for an individual A to hop from $\vec{r}$ to $\vec{r}'$ is given by $\epsilon z^{-1} a(\vec{r})[1-a(\vec{r}')]$ (for simplicity, we drop the time-dependence). Together with the reverse process, i.e. hopping from site $\vec{r}'$ to $\vec{r}$, this yields the non-diagonal part of $\mathcal{B}(\vec{r},\vec{r}')$ (see e.g. [10]):

$$\mathcal{B}(\vec{r},\vec{r}'\neq\vec{r}) = -\frac{\epsilon}{Nz}\big\{a(\vec{r})[1-a(\vec{r}')]+a(\vec{r}')[1-a(\vec{r})]\big\}\,. \tag{3.33}$$

Similarly, the diagonal entries of $\mathcal{B}$ read

$$\mathcal{B}(\vec{r},\vec{r}) = \frac{\epsilon}{Nz}\sum_{\text{n.n.}\vec{r}''}\big\{a(\vec{r})[1-a(\vec{r}'')]+a(\vec{r}'')[1-a(\vec{r})]\big\}\,, \tag{3.34}$$

where the sum runs over all nearest neighbors (n.n.) $\vec{r}''$ of the site $\vec{r}$. It follows from these expressions that

$$\begin{aligned}\mathcal{B}(\vec{r},\vec{r}') = \frac{\epsilon}{Nz}\sum_{\text{n.n.}\vec{r}''}&(\delta_{\vec{r},\vec{r}'}-\delta_{\vec{r}',\vec{r}''})\\ &\times\big\{a(\vec{r})[1-a(\vec{r}'')]+a(\vec{r}'')[1-a(\vec{r})]\big\}\,.\end{aligned} \tag{3.35}$$

In the continuum limit, with $\delta r\to 0$, we use the fact that $\delta_{\vec{r},\vec{r}'}\to\delta r^d\delta(\vec{r}-\vec{r}')$ and obtain

$$\begin{aligned}\mathcal{B}(\vec{r},\vec{r}') = \frac{\epsilon}{Nz}\delta r^d\sum_{\pm,i=1}^{d}&\big[\delta(\vec{r}-\vec{r}')-\delta(\vec{r}\pm\delta r\vec{e}_i-\vec{r}')\big]\\ &\times\big\{a(\vec{r})[1-a(\vec{r}\pm\delta r\vec{e}_i)]+a(\vec{r}\pm\delta r\vec{e}_i)[1-a(\vec{r})]\big\}\,.\end{aligned} \tag{3.36}$$

As in Eq. (**??**), we expand $\delta(\vec{r}\pm\delta r\vec{e}_i-\vec{r}')$ and $a(\vec{r}\pm\delta r\vec{e}_i)$ to second order and observe that only quadratic terms in δr do not cancel. With $\epsilon = DdN^{2/d}$ and $\delta r = N^{-1/d}$, we thus find:

$$\mathcal{B}(\vec{r},\vec{r}') = \frac{D}{N^2}\partial_{\vec{r}}\partial_{\vec{r}'}\big[\delta(\vec{r}-\vec{r}')a(\vec{r})(1-a(\vec{r})\big]. \tag{3.37}$$

The noise matrix $\mathcal{B}$ of the Fokker-Planck equation associated with the exchange processes therefore scales as N^{-2}. In the corresponding SPDE, the contribution to noise of the exchange processes scales like N^{-1}.

3.3.3 Stochastic partial differential equations

The comparison of snapshots obtained from lattice simulations with the numerical solutions of the SPDE reveals a remarkable coincidence of both approaches (see Fig. 3.5). Of course, due to the inherent stochastic nature of the interacting particle system, the snapshots do not match exactly for each realization. To reach a quantitative assessment on the validity of the SPDE (3.23) to describe the spatio-temporal properties of the system in the continuum limit, we have computed various correlation functions for the system's steady state. The attainment of the steady state is assessed by computing the long time evolution of the densities and various snapshots as those of Fig. 3.5. When the densities are found not to fluctuate significantly around their average values and the snapshots display statistically the same robust features at various times (typically

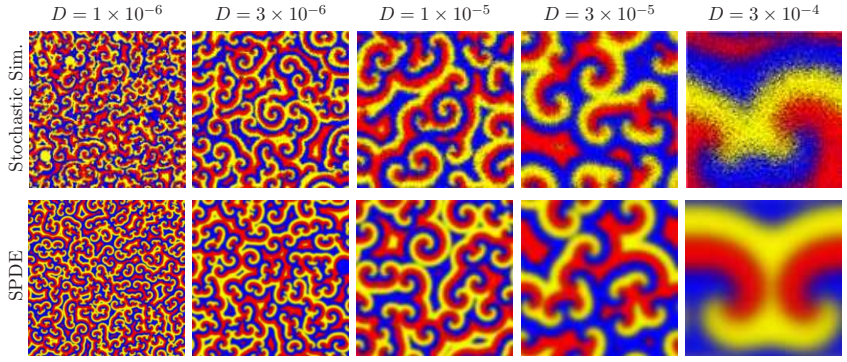

Figure 3.5: The reactive steady states. We show snapshots emerging in simulations of the interacting particle system (2.1) (top row) and obtained by solving the SPDE (3.23) (bottom row). Each color (level of gray) represents a different species (black dots denote empty spots). From left to right, the diffusion constant is increased from $D = 1 \times 10^{-6}$ to $D = 3 \times 10^{-4}$. The latter value is slightly below the critical threshold above which the spiral structures can no longer fit within the system [4]; see text. The system sizes used in the stochastic simulations are $L = 1000$ in the upper two panels, $L = 300$ for that at bottom, and $L = 500$ for the other two (middle). The selection and reproduction rates are chosen as $\sigma = \mu = 1$.

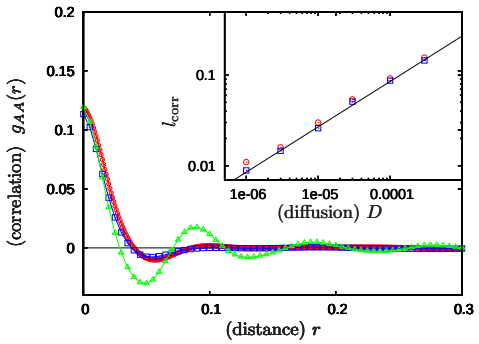

Figure 3.6: Correlation functions. The spatial correlation $g_{AA}(r)$ as function of r in the reactive steady state is shown. We report results obtained from stochastic simulations (red circles, for a lattice of linear size $L = 1000$) and numerical solutions of the SPDE (3.23), blue squares, and notice an excellent agreement. In both cases, results have been obtained for a value $D = 3 \times 10^{-6}$ and $\mu = \sigma = 1$. The typical correlation length $\ell_{\rm corr}$ as a function of the diffusion constant D is shown in the inset (on a double logarithmic scale). The scaling relation $\ell_{\rm corr} \sim \sqrt{D}$, indicated by a black line, is clearly confirmed. We have also reported the results for the static correlation function $g_{AA}(r)$ of the patterns predicted by the deterministic PDE (green triangles); see text. The latter are found to be markedly less damped than those arising in the stochastic descriptions of the system.

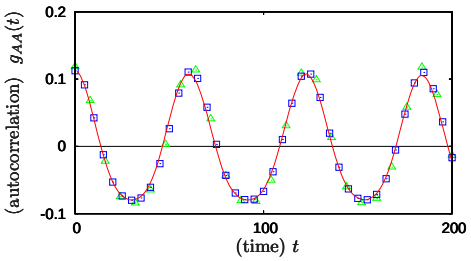

Figure 3.7: Autocorrelation. We show the correlation $g_{AA}(t)$ as a function of time t. Results from stochastic simulations (red/gray line) are compared with those obtained from the numerical solutions of the SPDE (blue squares), as well as with those computed from the deterministic PDE (green triangles). All results are in excellent agreement with each other and are characterized by oscillations at frequency $\Omega^{\rm num} \approx 0.103$ (for $\mu = \sigma = 1$); the latter is independent from the value of the diffusion D. These oscillations reflect the rotation of the spiral waves. The results from the SPDE and deterministic PDE have been obtained using $D = 10^{-5}$, while stochastic simulations have been performed on a lattice of length $L = 300$ with $D = 10^{-4}$.

$t \sim 100 - 1000$), the system is considered to be settled in its (reactive) steady state.

We first consider equal-time correlation functions, which yield information about the size of the emerging spirals. As an example, we focus on the correlation $g_{AA}(|\vec{r} - \vec{r}'|)$ at $\vec{r}$ and $\vec{r}'$ of the subpopulation A, $g_{AA}(|\vec{r} - \vec{r}'|) = \langle a(\vec{r}, t)a(\vec{r}', t)\rangle - \langle a(\vec{r}, t)\rangle\langle a(\vec{r}', t)\rangle$. Here, the brackets $\langle ...\rangle$ stand for an average over all histories. In the steady state, the time dependence drops out and, because of translational and rotational invariance, the latter depends only on the separating distance $|\vec{r} - \vec{r}'|$. In Fig. 3.6, we report results for g_{AA} obtained from lattice simulations (red circles) and from numerical solutions of the SPDE (3.23) (blue squares), finding an excellent agreement between them. When the separating distance vanishes, the correlation reaches its maximal value and then decreases, exhibiting (damped) spatial oscillations. The latter reflect the underlying spiralling spatial structures, where the three subpopulations alternate in turn. Damping results from the averaging over many small spirals. As described in the previous subsection, the correlation functions are characterized by their correlation length $\ell_{\rm corr}$, which conveys information on the typical size of the spirals. In the inset of Fig. 3.6, we show the dependence of the correlation length on the diffusion rate D in a double logarithmic plot which confirms the scaling relation $\ell_{\rm corr} \sim \sqrt{D}$, also inferred from general considerations.

We now consider the time dependence of the correlation functions and study the autocorrelation $g_{AA}(|t - t'|)$ of subpopulation A at times t and t', for a fixed spatial position. This quantity is given by $g_{AA}(|t - t'|) = \langle a(\vec{r}, t)a(\vec{r}, t')\rangle - \langle a(\vec{r}, t)\rangle\langle a(\vec{r}, t')\rangle$ and only depends on the time difference $|t - t'|$. Both lattice simulations and SPDE (3.23) yield oscillating correlation functions, as shown in Fig. 3.7. This periodic behavior, with a frequency numerically found to be $\Omega^{\rm num} \approx 0.103$ (for $\sigma = \mu = 1$), stems from the rotational nature of the spiral waves and is independent of the diffusion constant D. Below, this value is compared with an analytical prediction inferred from a deterministic description of the spatial system. In the time intervals which we have investigated, $t \sim$

1,000, the oscillations, as reported in Fig. 3.7, are undamped. Therefore, on this time-scale, the position of the spirals' vortices is stable in the steady state and not influenced by noise. On larger time-scales, however, we expect the vortices to perform random walks (see [5] for a general discussion as well as [11, 12] for investigations of vortex dynamics in rock-paper-scissors models), with associated vortex annihilation and creation processes. Studies exploring such a behavior are promising for further broadening the understanding of stochastic effects on nonequilibrium steady state.

3.3.4 The spirals' velocities, wavelengths, and frequencies

Above, we have found that characteristic properties of the emerging spiral waves, like their wavelength and frequency, are unaffected by noise. To compute these quantities analytically, it is therefore not necessary to take noise into account, and we may focus on the study of the deterministic PDE (**??**). In Subsection **??**, we show how the dynamics of the latter is essentially captured by an appropriate complex Ginzburg-Landau equation (CGLE), given by Eq. (3.3) for the case under consideration here. The CGLE (3.3) allows to derive analytical results for the emergence of spiral waves, their stability and their spreading velocity, as well as their wavelength and frequency. We detail these findings in Subsections **??** and 3.2.2. Here, we assess the accuracy and validity of these analytical predictions by comparing them with values obtained from the numerical solutions of the SPDE (3.23).

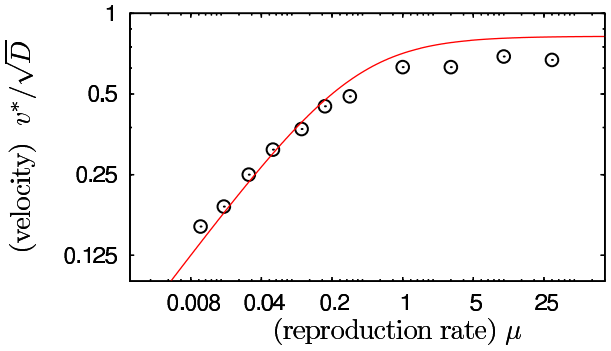

Figure 3.8: Spreading velocity. We report the dependence of front velocity v^* (rescaled by a factor $\sqrt{D}$) on the reproduction rate μ. The time scale is set by keeping $\sigma = 1$. In red (full line), we report the analytical predictions (3.14) obtained from the CGLE, which are compared with numerical results (black dots). The latter are obtained from the numerical solutions of the SPDE (3.23).

Let us first consider the spreading velocity v^* of the emerging wave fronts. The analytical value, inferred from the CGLE (3.3) and derived in Subsection **??** [see Eq. (3.14)], reads $v^* = 2\sqrt{c_1 D}$, where $c_1 = \mu\sigma/[2(3\mu + \sigma)]$ is a coefficient appearing in the CGLE (3.3). In numerical computations, the front velocity is obtained from the wavelength λ and the frequency Ω of the emerging spirals. Namely, the wavelength $\lambda^{\rm num}$ can be inferred from snapshots (as in Fig. 3.5), and the frequency $\Omega^{\rm num}$ is computed from the oscillations of the autocorrelation (as in Fig. 3.7). The velocity then follows via $v^{\rm num} = \lambda^{\rm num}\Omega^{\rm num}/2\pi$. As the

wavelength is proportional to $\sqrt{D}$ and the frequency does not depend on the diffusion constant, one can easily check that the relation $v^{\rm num} = \lambda^{\rm num}\Omega^{\rm num}/2\pi$ confirms that $v^{\rm num} \sim \sqrt{D}$, as in Eq. (3.14). In Fig. 3.8, we compare the analytical prediction (3.14) for v^* with results obtained from the numerical solution of the SPDE (3.23), as function of the reproduction rate μ (setting $\sigma = 1$, we fix the time scale), and find a good agreement. On the one hand, for small values of μ (much lower than the selection rate, $\mu \ll 1$), reproduction is the dominant limiter of the spatio-temporal evolution. In the limit $\mu \to 0$, the front velocity therefore only depends on μ. From dimensional analysis, it follows $v^* \sim \sqrt{\mu}$, as also confirmed by the analytical solution Eq. (3.14). On the other hand, if reproduction is much faster than selection, $\mu \gg 1$, the latter limits the dynamics, and we recover $v^* \sim \sqrt{\sigma}$. In Fig. 3.8, as $\sigma = 1$, this behavior translates into v^* being independent of μ in this limit. While the numerical and analytical results coincide remarkably for low reproduction rates (i.e. $\mu \leq 0.3$), systematic deviations ($\approx 10\%$) appear at higher values. As an example, when selection and reproduction rates are equal, $\sigma = \mu = 1$ (as was considered throughout the last section), we have numerically found a velocity $v^{\rm num} \approx 0.63\sqrt{D}$, while Eq. (3.14) yields the analytical result $v^* = \sqrt{D/2} \approx 0.71\sqrt{D}$.

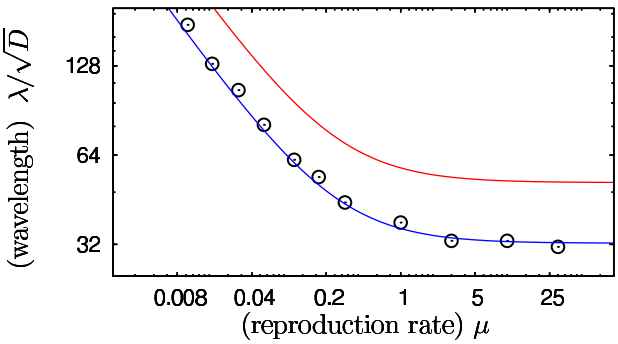

Figure 3.9: The spirals' wavelength. We show the functional dependence of the wavelength λ on the rate μ (with $\sigma = 1$), and compare numerical results (black circles), obtained from the numerical solutions of the SPDE (3.23), to analytical predictions (red line). The latter stem from the CGLE and are given by Eq. (3.20). They differ from the numerics by a factor of 1.6, see text. Adjusting this factor, c.f. the blue line, the functional dependence is seen to agree very well with numerical results.

Concerning the spirals' wavelengths and frequencies, in Subsection 3.2.2, we analytically infer predictions from the CGLE (3.3) given by Eqs. (3.19) and (3.20). We have checked these results against numerical computations. In Fig. 3.9, the analytical estimates for the wavelength λ are compared with those obtained from the numerical solution of the SPDE (3.23) for different values of the reproduction rate μ. We notice that there is an excellent agreement between analytical and numerical results for the functional dependence of λ on μ. For low reproduction rates ($\mu \ll 1$) we have $\lambda \sim 1/\sqrt{\mu}$, while when reproduction occurs much faster than selection ($\mu \gg 1$), the dynamics is independent of μ and $\lambda \sim 1/\sqrt{\sigma}$. We have also found that the analytical result predicts an amplitude of λ which exceeds that obtained from numerical computations by a constant factor ≈ 1.6, taken into account in Fig. 3.9. We attribute this devia-

tion to the fact that the CGLE (3.3) (stemming from the normal form (2.22)) describes a dynamics exhibiting a limit cycle, while the full May-Leonard rate equations (2.2) are characterized by heteroclinic orbits. The correct functional dependence of the wavelength λ on the reproduction rate μ is therefore especially remarkable. Elsewhere it will be shown that in the presence of mutations, inducing a limit-cycle behavior, the description of the emerging spiral waves in terms of CGLE (3.3) becomes fully accurate.

For the spirals' frequency, we analytically obtain $\Omega = \Omega(q^{\rm sel}) = \omega + 2(c_1/c_3)\left(1-\sqrt{1+c_3^2}\right)$, see Subsection 3.2.2. As already inferred from numerical simulations (Sec. III.B), Ω does not depend on the diffusion D. Quantitatively, and as an example for $\mu = \sigma = 1$, we obtain the analytical prediction $\Omega \approx 0.14$, which differs by a factor ≈ 1.4 from the numerical value $\Omega^{\rm num} \approx 0.103$ found in Fig. 3.7. As for the wavelength, this difference stems from the fact that the May-Leonard rate equations (2.2) predict heteroclinic orbits approaching the boundaries of the phase space, while the dynamics underlying the CGLE is characterized by limit cycles (usually distant from the edges of the phase space) resulting from a (supercritical) Hopf bifurcation.

3.3.5 Scaling relation and critical mobility

An important question is to understand what is the mechanism driving the transition from a stable coexistence to extinction at the critical mobility D_c. To address this issue, we first note that varying the mobility induces a scaling effect, as illustrated in Fig. 3.3. In fact, increasing the diffusion D results in zooming into the system. As discussed above, the system's dynamics is described by a set of suitable stochastic partial differential equations (SPDE) whose basic properties help rationalize this scaling relation. In fact, the mobility enters the stochastic equations through a diffusive term $D\Delta$, where Δ is the Laplace operator involving second-order spatial derivatives. Such a term is left invariant when D is multiplied by a factor α while the spatial coordinates are rescaled by $\sqrt{\alpha}$. It follows from this reasoning that varying D into αD translates in a magnification of the system's characteristic size by a factor $\sqrt{\alpha}$ (say $\alpha > 1$). This implies that the spirals' wavelength λ is proportional to $\sqrt{D}$ (i.e. $\lambda \sim \sqrt{D}$) up to the critical D_c .

When the spirals have a critical wavelength λ_c, associated with the mobility D_c, these rotating patterns outgrow the system size which results in the loss of biodiversity. In the "natural units" (length is measured in lattice size units and the time-scale is set by keeping $\sigma = 1$), we have numerically computed $\lambda_c = 0.8 \pm 0.05$. This quantity has been found to be universal, i.e. its value remains constant upon varying the rates σ and μ. However, this is not the case of the critical mobility D_c, which depends on the parameters of the system. Below the critical threshold D_c, the dynamics is characterized by the formation of spirals of wavelength $\lambda(\mu, D) \sim \sqrt{D}$. This relation, together with the universal character of λ_c, leads to the following equation:

$$D_c(\mu) = \left(\frac{\lambda_c}{\lambda(\mu, D)}\right)^2 D \ , \tag{3.38}$$

which gives the functional dependence of the critical mobility upon the system's parameter. To obtain the phase diagram reported in Fig. 3.10 we have

used Eq. (3.38) together with values of $\lambda(\mu, D)$ obtained from numerical simulations. For computational convenience, we have measured $\lambda(\mu, D)$ by carrying out a careful analysis of the SPDE's solutions. The results are reported as black dots in Fig. 3.10. We have also confirmed these results through lattice simulations for systems with different sizes and the results are shown as blue dots in Fig. 3.10. Finally, we have taken advantage of the analytical expression (up to a constant prefactor, taken into account in Fig. 3.10) of $\lambda(\mu, D)$ derived from the complex Ginzburg-Landau equation (CGLE) associated with the system's dynamics: with Eq. (3.38), we have obtained the red curve displayed in Fig. 3.10. This figure corroborates the validity of the various approaches (SPDE, lattice simulations and CGLE), which all lead to the same phase diagram where the biodiverse and the uniform phases are identified.

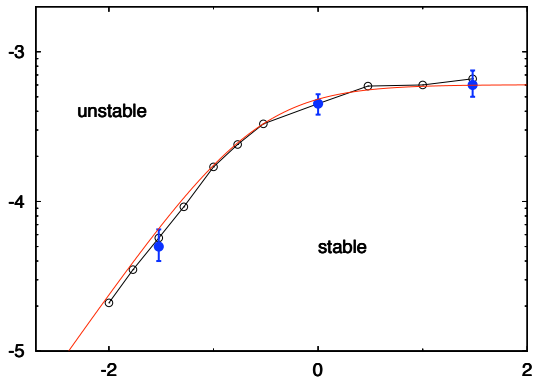

Figure 3.10: Phase diagram. The critical diffusion constant D_c as a function of the reproduction rate μ yields a phase diagram with a phase where biodiversity is maintained as well as a uniform one where two species go extinct. Time unit is set by $\sigma = 1$. On the one hand, we have computed D_c from lattice simulations, using different system sizes. The results are shown as blue crosses. On the other hand, we have calculated D_c using the approach of stochastic PDE (black dots, black lines are a guide to the eye) as well as analytically via the complex Ginzburg-Landau equation (red line). Varying the reproduction rate, two different regimes emerge. If μ is much smaller than the selection rate, i.e. $\mu \ll \sigma$, reproduction is the dominant limiter of the temporal development. In this case, there is a linear relation with the critical mobility, i.e. $D_c \sim \mu$, as follows from dimensional analysis. In the opposite case, if reproduction occurs much faster than selection ($\mu \gg \sigma$), the latter limits the dynamics and D_c depends linearly on σ, i.e. $D_c \sim \sigma$. Here, as $\sigma = 1$ is kept fixed (time-scale unit), this behaviour reflects in the fact that D_c approaches a constant value for $\mu \gg \sigma$.

3.4 Discussion

Individuals' mobility as well as intrinsic noise have crucial influence on the self-formation of spatial patterns. We have quantified their influence by investigating a stochastic spatial model of mobile individuals experiencing cyclic dominance via interactions of 'rock-paper-scissors' type. We have demonstrated that individuals' mobility has drastic effects on the emergence of spatio-temporal pat-

terns. Low exchange rate between neighboring individuals leads to the formation of small and irregular patterns. In this case coexistence of all subpopulations is preserved and the ensuing patterns are mainly determined by stochastic effects. On the other hand, in two dimensions, larger exchange rates (yet of same order as the reaction rates) yield the formation of (relatively) regular spiral waves whose rotational nature is reminiscent of the cyclic and out-of-equilibrium ensuing kinetics. In fact, the three subpopulations endlessly, and in turn, hunt each other. The location and density of the spirals' vortices is either determined by initial spatial inhomogeneities, if these take pronounced shape, or by stochasticity. In the latter case, internal noise leads to an entanglement of many small spirals and a universal vortex density of about 0.5 per square wavelength. Increasing the diffusion rate (i.e. individuals' mobility), the typical size of the spiral waves rises, up to a critical value. When that threshold is reached, the spiral patterns outgrow the two-dimensional system and there is only one surviving subpopulation covering uniformly the system [4].

The language of interacting particles enabled us to devise a proper treatment of the stochastic spatially-extended system and to reach a comprehensive understanding of the resulting out-of-equilibrium and nonlinear phenomena. In particular, we have shown how spatio-temporal properties of the system can be aptly described in terms of stochastic partial differential equations (SPDE) and confirmed our findings with lattice simulations. We have paid special attention to analyze the wavelength and frequency of the spiral waves, as well as the velocity of the propagating fronts. Numerical solutions of the SPDE have been shown to share (statistically) the same steady states as the lattice simulations, with the emerging spiral waves characterized in both cases the same wavelength, overall sizes and frequency. We have also studied the influence of stochasticity on the properties of the coexistence state and its spatio-temporal structure. Namely, we have compared the results obtained from the SPDE with those of the deterministic PDE (obtained by dropping the noise contributions in the SPDE), which still yield spiralling structures. This allowed us to shed light on the fact that, in the presence of (sufficient) mobility, the wavelength and frequency of the spirals are not affected by internal noise. However, there are major differences between the stochastic and deterministic descriptions of the system. One of the most important is the influence of the initial conditions. On the one hand, if initial spatial inhomogeneities are larger than the noise level, or if noise is absent as in the deterministic descriptions, these initial spatial structures determine the position of the spirals' vortices. In this situation, the system "memorizes" its initial state, and the latter crucially influences the overall size of the emerging spiral waves. On the other hand, for rather homogeneous initial densities (at values of the unstable reactive fixed point), the patterns emerging from the stochastic descriptions (lattice simulations and SPDE) are caused by noise and characterized by a universal density of 0.5 spiral vortices per square wavelength. While we have provided qualitative explanations of these findings, a more profound understanding is still desirable and could motivate further investigations.

We have also shown that analytical expressions for the spirals' wavelength and frequency can be determined by means of a complex Ginzburg-Landau equation (CGLE) obtained by recasting the PDE of the system, restricted onto an invariant manifold, in a normal form. There is good agreement between analytical predictions stemming from the system's CGLE and the numerical

results (obtained from stochastic lattice simulations as well as the numerical solution of the SPDE). This can be traced back to the fact that May-Leonard rate equations are characterized by heteroclinic orbits very much reminiscent of limit cycles resulting from a Hopf bifurcation. The fact that the dynamics can be recast in the form of a CGLE, known to give rise to the emergence of coherent structures, reveals the generality of the phenomena discussed in this work and greatly facilitates their quantitative analysis. In particular, the emergence of an entanglement of spiral waves in the coexistence state, the dependence of spirals' size on the diffusion rate, and the existence of a critical value of the diffusion above which coexistence is lost are robust phenomena. This means that they do not depend on the details of the underlying spatial structure: While, for specificity, we have (mostly) considered square lattices, other two-dimensional topologies (e.g. hexagonal or other lattices) will lead to the same phenomena, too. Also the details of the cyclic competition have no qualitative influence, as long as the underlying rate equations exhibit an unstable coexistence fixed point and can be recast in the universality class of the Hopf bifurcations. We still note that instead of defining the model in terms of chemical reactions, as done here (2.1), we can equivalently choose a formulation in terms of payoff matrices [13, 2].

We have investigated the system's behavior in two spatial dimensions. However, our approach, using a continuum limit to derive the SPDE (3.23) as well as the CGLE (3.3), is equally valid in other dimensions and expected to describe the formation of spatial patterns, as long as the mobility is below a certain threshold value [4]. As examples, in one dimension, the CGLE yields traveling waves, while "scroll waves", i.e. vortex filaments, result in three dimensions [6].

In these lecture notes, we have mainly focused on the situation where the exchange rate between individuals is sufficiently high, which leads to the emergence of regular spirals in two dimensions. However, when the exchange rate is low (or vanishes), we have seen that stochasticity strongly affects the structure of the ensuing spatial patterns. In this case, the (continuum) description in terms of SPDE breaks down. In this situation, the quantitative analysis of the spatio-temporal properties of interacting particle systems requires the development of other analytical methods, e.g. relying on field theoretic techniques [14]. Fruitful insights into this regime have already been gained by pair approximations or larger-cluster approximations [11, 15, 16, 17]. The authors of these studies investigated a set of coupled nonlinear differential equations for the time evolution of the probability to find a cluster of certain size in a particular state. While such an approximation improves when large clusters are considered, unfortunately the effort for solving their coupled equations of motion also drastically increases with the size of the clusters. In addition, the use of those cluster mean-field approaches becomes problematic in the proximity of phase transitions (near an extinction threshold) where the correlation length diverges. Investigations along these lines represent a major future challenge in the multidisciplinary field of complexity science.

Bibliography

[1] R. M. May and W. J. Leonard, SIAM J. Appl. Math **29**, 243 (1975).

[2] J. Hofbauer and K. Sigmund, *Evolutionary Games and Population Dynamics* (Cambridge University Press, ADDRESS, 1998).

[3] S. Wiggins, *Introduction to Applied Nonlinear Dynamical Systems and Chaos*, 1st ed. (Springer, ADDRESS, 1990).

[4] T. Reichenbach, M. Mobilia, and E. Frey, Nature **448**, 1046 (2007).

[5] M. C. Cross and P. C. Hohenberg, Rev. Mod. Phys. **65**, 851 (1993).

[6] I. S. Aranson and L. Kramer, Rev. Mod. Phys. **74**, 99 (2002).

[7] W. v. Saarloos, Phys. Rep. **386**, 29 (2003).

[8] N. G. van Kampen, *Stochastic processes in physics and chemistry*, 1st ed. (North Holland Publishing Company, ADDRESS, 1981).

[9] C. W. Gardiner, *Handbook of Stochastic Methods*, 1st ed. (Springer, ADDRESS, 1983).

[10] U. C. Täuber, graduate textbook (work in progress): Critical Dynamics (2008) `http://www.phys.vt.edu/~tauber`.

[11] K. Tainaka, Phys. Rev. E **50**, 3401 (1994).

[12] H. Nishiuchi, N. Hatano, and K. Kubo, Phys. A **387**, 1319 (2008).

[13] J. Maynard Smith, *Evolution and the Theory of Games* (Cambridge University Press, ADDRESS, 1982).

[14] M. Mobilia, I. T. Georgiev, and U. C. Täuber, J. Stat. Phys. **128**, 447 (2007).

[15] K. Sato, N. Konno, and T. Yamaguchi, Mem. Muroran Inst. Tech. **47**, 109 (1997).

[16] G. Szabó, A. Szolnoki, and R. Izsak, J. Phys. A: Math. Gen. **37**, 2599 (2004).

[17] G. Szabó and G. Fath, Phys. Rep. **446**, 97 (2007).